Dynamics of Atmospheres and Oceans 48 (2009) 93–120

Contents lists available at ScienceDirect

Dynamics of Atmospheres and Oceans

journal homepage: www.elsevier.com/locate/dynatmoce

Baroclinic tidal generation in the Kauai Channel inferred from high-frequency radio Doppler current meters

Edward D. Zaron[a,*], Cedric Chavanne[b,1], Gary D. Egbert[c], Pierre Flament[b]

[a] Department of Civil and Environmental Engineering, Portland State University, P.O. Box 751, Portland, OR 97207-0751, United States
[b] School of Ocean and Earth Science and Technology, University of Hawai'i, United States
[c] College of Oceanic and Atmospheric Sciences, Oregon State University, United States

ARTICLE INFO

Article history:
Available online 5 April 2009

Keywords:
Tidal modeling
Data assimilation
Tidal conversion

ABSTRACT

A data-assimilating three-dimensional primitive equations model is used in conjunction with high-frequency radio Doppler current data to infer tidal conversion during two 3-month periods in Kauai Channel, Hawaii. It is estimated that the M_2 barotropic tide loses energy at rates of 1.1 and 1.2 GW during these periods, values 25% lower than predicted with the prior model. Of this total conversion rate, approximately 85% exits the model domain to enter the deep ocean as a coherent propagating internal tide. Although the inferred tidal currents differ in detail during the 3-month periods, the domain-averaged tidal energetics do not. The tidal solutions obtained by the data-assimilative model do not exactly satisfy the primitive equations dynamics since a residual forcing is permitted in the horizontal momentum and mass conservation equations. An analysis of these residuals indicates that they are consistent with the expected amplitude of tidal-mesoscale interactions; however, the residual forcing in the mass equation, which represents refraction by the mesoscale buoyancy field, is much too small. An attempt to reconcile the forcing residuals with known processes suggests, by elimination, that tidal-mesoscale interactions are of leading-order significance and should be included in future analysis of baroclinic tidal energy budgets.

* Corresponding author.
E-mail address: zaron@cee.pdx.edu (E.D. Zaron).
[1] Present address: University of East Anglia, Norwich, United Kingdom.

0377-0265/$ – see front matter © 2009 Elsevier B.V. All rights reserved.
doi:10.1016/j.dynatmoce.2009.03.002

1. Introduction

The analysis of long time series of satellite altimeter observations has demonstrated that the barotropic or surface tide dissipates roughly 3.5 TW of energy, of which roughly two-thirds is lost to frictional processes in the shallow coastal ocean (Egbert and Ray, 2000, 2001). The remaining energy dissipation occurs in the open ocean where it may play an important role in maintaining and regulating the oceans' meridional overturning circulation (Munk and Wunsch, 1998; Simmons et al., 2004b). Additional evidence for the global importance of deep ocean tidal dissipation is found in tidal model studies which incorporate loss of barotropic energy either by parameterization (Jayne and St. Laurent, 2001) or by direct simulation of baroclinic tidal generation at rough topography (Arbic et al., 2004).

The extent to which tidal dissipation contributes to the meridional overturning circulation depends largely on where tidal mixing and the associated vertical buoyancy flux occurs. In the deep ocean it has been assumed that the vast majority of energy loss from the surface tide occurs where the barotropic tide flows across the bathymetric gradient, periodically forcing the isopycnals to deviate from the horizontal (Baines, 1982). Near a large-scale geomorphic feature like the Hawaiian Ridge, this conversion process extracts roughly 10% of the energy from the propagating barotropic tide (Zaron and Egbert, 2006a, 2007), and results in the generation of a baroclinic or internal tide. A portion of this energy is lost to turbulence via rapid nonlinear interactions near the conversion site (Klymak et al., 2008; Levine and Boyd, 2006), with the remainder propagating as a phase-coherent low-mode internal tide, which observations indicate can propagate for 1000's of kilometers in the deep ocean (Ray and Mitchum, 1996, 1997; Alford, 2003). The precise partitioning of energy into locally dissipated and propagating components depends in detail on the structure of the bathymetric features, with smaller-scale elements, such as are found on the mid-Atlantic Ridge, leading to more high-mode generation and local mixing (St. Laurent and Nash, 2004). For an overview of the literature, the reader is referred to the recent review by Garrett and Kunze (2007).

Our goal here is to partition the energy lost from the surface tide into locally dissipated and propagating components for a relatively well-studied site, namely, Kauai Channel, between the islands of Oahu and Kauai in the Hawaiian Archipelago. This location was originally identified as a generation site of the baroclinic tide from observations (Ray and Mitchum, 1997) and modeling studies (Merrifield and Holloway, 2002), and a number of studies from the Hawaii Ocean Mixing Experiment (HOME) were focussed here (Rudnick et al., 2003; Lee et al., 2006; Carter and Gregg, 2006; Nash et al., 2006).

No single observation or set of observations contains enough information to unambiguously close the tidal energy budget in the region enclosing Kauai Channel. Measurements indicate that turbulence and mixing is spatially variable and depends strongly on the phase of the spring-neap cycle (Carter and Gregg, 2006; Klymak et al., 2006). Other observations have shown that the structure of the propagating tide is spatially complex (Lee et al., 2006; Nash et al., 2006), with a three-dimensional structure resulting from the orientation of the barotropic tidal currents and the local bathymetry. The studies cited have used numerical models to assist in interpreting and quantifying tidal processes in the Channel; however, there is considerable challenge in accomplishing this on even a local scale. First, barotropic to baroclinic conversion is most efficient over steep slopes, so very high-resolution numerical models and bathymetric data are necessary (Zaron and Egbert, 2006b; Carter et al., 2008). Second, the influence of the subgrid-scale turbulence parameterizations on the resolved scales is poorly understood, and it is not known to what degree the extant turbulence closures represent observed processes such as large-scale internal wave breaking (Legg and Huijts, 2006). Third, the impact of three-dimensional non-tidal variations in buoyancy and velocity, e.g., the mesoscale and sub-mesoscale, are difficult to incorporate in models since these fields are normally unknown at the scale of the internal tide.

A natural way to address these challenges is to consider data assimilative modeling, rather than conventional prognostic modeling. This approach uses a dynamical model which approximately governs the tide together with a description for the amplitude and correlation structure of the acknowledged errors in the model. Using standard methods of variational data assimilation (Bennett, 2002), tidal fields are found which minimize a weighted sum of squared model error and data errors, where the weights are derived from the hypothesized errors in each. The results of the data assimilative approach are, (1) improved estimates of the tidal fields and estimates of errors in the model, and (2) a test of the validity of the hypothesized model and its assumed errors.

Here we use a data-assimilating primitive equations model to infer the complete three-dimensional tidal fields from surface velocity data obtained with two high-frequency radio (HFR) Doppler current meters. The HFRs, their directional (beam-forming) capabilities and other characteristics are described in detail in Chavanne et al. (submitted for publication-a). These data are unique because they permit an examination of tidal processes from synoptic data at a site of intense baroclinic energy conversion, and they are one of the few kinds of data with both the temporal and spatial resolution to simultaneously observe tidal and non-tidal (mesoscale) phenomena. The numerical model, PEZ-HAT, utilizes simplified dynamics in which non-hydrostatic motions are filtered out and the nonlinearities are neglected, except in-so-far as the turbulence has been parameterized by down-gradient transport of buoyancy and momentum. The temporal structure of the model is also reduced by considering just the dominant semidiurnal tidal constituent M_2. We take this simplified approach because of the pragmatic difficulties associated with modeling the complete, multi-constituent, tidal fields and the mesoscale simultaneously.

Our objective is to estimate the three-dimensional tidal fields during the two 3-month periods between August 2002 and May 2003 when both HFRs were functioning. We find that the observed tidal velocities are smaller than those from the prior (data-less) model, and there is less horizontal shear in the observations compared to the model. In contrast, the data assimilative model is able to nearly interpolate the observations, assuming a plausible scaling for the tidal-mesoscale interactions. The inferred interaction is in the sense of a reduction of tidal energy radiated to the deep ocean, but the magnitude of the effect is small compared to uncertainty in the model. The HFR data provide evidence to support of the hypothesis that the generation of the internal tide is influenced by the wind-driven mesoscale circulation. The present analysis does not permit us to distinguish the differing contributions of turbulence vs. tidal-mesoscale interactions. A more complete analysis must consider the mesoscale separately, a problem which is left for future research.

2. Data and methods

2.1. Data

Two high frequency radio (HFR) transceivers measured ocean surface velocities for 9 months (August 30, 2002 to May 22, 2003) in the Kauai Channel, a narrow region between O'ahu Island and Kauai Island in the Hawaiian Archapelago in the North Pacific Ocean. Each HFR consisted of transmit antennas, an array of 16 receive antennas, and the signal processing equipment necessary for beam-forming. Ocean surface currents were inferred from the Doppler shift of the Bragg scattering by ocean surface waves (Gurgel et al., 1999). The systems were operated with a nominal range of approximately 75 km, a range resolution of 1.5 km, and an angular resolution of 7°. The reader is referred to Chavanne et al. (submitted for publication-a) for a more detailed description of the HFR instrumentation and data.

The HFR transceivers were located at Ka'ena Point (KP) and at Ko'Olina Harbor (KO). The antenna array at KP was inadvertently jammed by a Navy transmission from December 8, 2002 to February 19, 2003, during which time no usable data were recovered from this array. Data used in this study come from two 3-month periods, P1: August 30, 2002–December 7, 2002, and P2: February 20, 2003–May 22, 2003, when both of the antenna arrays were functioning. During these two periods time series of hourly averaged radial velocity at each point in the observational arrays were harmonically analyzed to extract the complex amplitude of the dominant semidiurnal tide, M_2 (Pawlowicz et al., 2002), and it is these harmonic constants that are assimilated by the model.

The harmonic constants for radial velocities show consistent phase propagation from the ridge towards the southwest (see Fig. 1), with a complex amphidromic structure on the south flank of the ridge. The change in M_2 amplitude between the two periods is substantial (10 cm/s) and well exceeds the expected error (1 cm/s). Note that the dominant semidiurnal frequencies, M_2 and S_2, are well-separated by the harmonic analysis of the 3-month time series.

The first period (P1) is characterized by M_2 current amplitudes from 16 to 20 cm/s off the ridge in deep water. During this time, a northward mean flow of 30 cm/s was observed at the surface, and anticyclonic relative vorticity values were typically $-0.3f$. Contemporaneous moored ADCP current

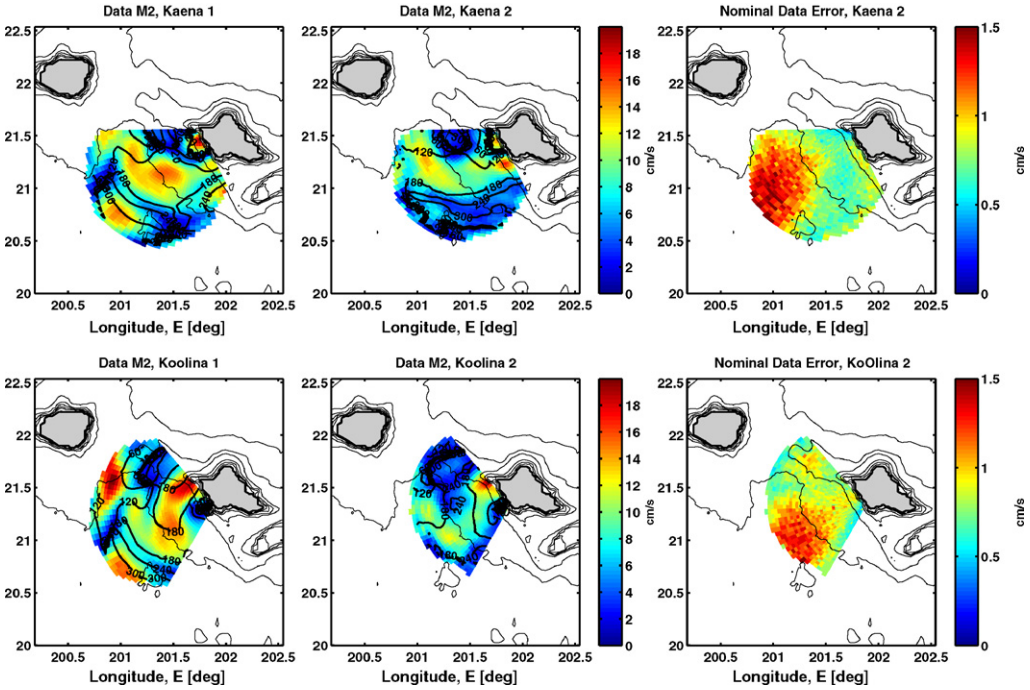

Fig. 1. M_2 radial velocity inferred from HFR. Complex harmonic constants for the M_2 component of the radial velocity are show for the Ka'ena Point (top row) and Ko'Olina (top row) antenna arrays. The left and center columns show data from the two time periods, P1 and P2, respectively. The right column shows the nominal error estimate in the harmonic constants for P2 (similar amplitude for P1, not shown).

measurements indicate that the mean flow was strongly sheared in the upper 300 m (Chavanne et al., submitted for publication-a).

During P2, the non-tidal currents were oriented more nearly north–northwest, and there was less vertical shear. Relative vorticity was generally anticyclonic, with a value of $-0.4f$ near shore (Chavanne et al., submitted for publication-a). Peak currents of 40 cm/s were found further offshore than during P1.

The relationship between the mesoscale and tidal currents is complex and discussed more fully in Chavanne et al. (submitted for publication-b). As a guide to the possible interactions, consider the properties of M_2 internal waves vs. the slowly varying, non-tidal, flow. Table 1 presents the wavelength (L), phase velocity (c_p), and group velocity (c_g) of the first four internal modes at the semidiurnal frequency, based on the time-average Brunt-Vaisala frequency at Station Aloha during P1 and P2 (Fujieki et al., 2006), in water of depth 4000 m and 400 m. In the deep water (4000 m), there is a clear separation between the tidal phase speed (0.75–3 m/s) and the mesoscale advective speed (approx. 0.25 m/s), so the low modes ought to be relatively unaffected by the non-tidal currents (Rainville and Pinkel, 2006).

Table 1
M_2 internal modes.

4000 m depth					400 m depth		
Mode	L [km]	c_p [m/s]	c_g [m/s]	ν^2	L [km]	c_p [m/s]	c_g [m/s]
1	145	3.2	2.8	3.0×10^{-2}	40	0.90	0.79
2	71	1.6	1.4	1.1×10^{-1}	21	0.48	0.42
3	47	1.1	0.92	2.3×10^{-1}	13	0.29	0.26
4	35	0.79	0.69	3.9×10^{-1}	10	0.22	0.19

Conversely, in 400 m deep water over Kaena Ridge, modes two and higher will likely interact strongly with the mesoscale, as the phase speed of the tide is within a factor of two of the mesoscale, and the length scales are commensurate (assuming 50 km length scale for the non-tidal flow, Chavanne et al., submitted for publication-b). Thus, in addition to the modal conversion and dispersion due to propagation over steeply sloping topography, conversion and dispersion due to interaction with the mesoscale should be expected.

2.2. Primitive equations model: PEZ-HAT

PEZ-HAT is a numerical model that was developed specifically for data-assimilative studies of the internal tide over complex bathymetry. The model name, PEZ-HAT, an acronym for "Primitive Equations Z-coordinate–Harmonic Analysis Tides," reflects the fact that PEZ-HAT is composed of two components: (1) PEZ: a primitive equations model closely based on the Geophysical Fluid Dynamics Laboratory Modular Ocean Model, version-3 (GFDL MOM3, Pacanowski and Griffies, 1999), and (2) HAT: a set of software modules to implement the astronomical tidal forcing (with corrections for the Earth load tide and ocean self-attraction, Egbert and Erofeeva, 2002), open boundary conditions, and harmonic analysis of the solutions. While PEZ is based on the MOM3 numerics, it was coded from scratch to utilize parallel domain decomposition techniques and facilitate coding of its adjoint model, which is necessary for our intended variational data-assimilative applications. PEZ utilizes partial-cell topography (Pacanowski and Gnanadesikan, 1998) and a squared-cosine time-averaging kernel for the split explicit barotropic time stepping algorithm (Shchepetkin and McWilliams, 2005). For more details of the numerical implementation, the reader is referred to Zaron and Egbert (2006b).

In the present application, PEZ-HAT is configured as a solver for the primitive equations linearized around a horizontally uniform background state, and the turbulence mixing coefficients are set to small, constant values. The purpose of both these simplifications is to isolate the tidal fields which can be modeled accurately, without the confounding influences of nonlinearity (both tidal-mesoscale and tidal self-interactions) or complex turbulence parameterization. In principle, the model could have been integrated with a horizontally varying background state; however, absent a credible estimate for the horizontal buoyancy field, this was not attempted. We have sought to infer the nonlinear and dissipative dynamics from the data assimilative solutions, rather than via direct numerical simulations.

Solutions to the prior, non-data-assimilating, version of PEZ-HAT are shown below and in Chavanne et al. (submitted for publication-a). They are obtained by time-stepping the linearized primitive equations in a regional domain centered on Kauai Channel. Boundary conditions are set by specifying the normal component of the barotropic transport on open boundaries. The baroclinic velocity and tracer fields use a Sommerfeld radiation condition based on the mode-1 internal wave phase speed at open boundaries (Pearson, 1974). Used alone, these boundary conditions would lead to spurious reflections of the higher modes, so a sponge layer is also used in which Newtonian damping and Laplacian mixing coefficients are ramped up towards the boundary. Very high resolution is necessary to quantitatively simulate baroclinic tidal dynamics Zaron and Egbert (2006b), and the present model uses a horizontal resolution of 2 km and a vertical resolution that varies from 30 m at the ocean surface to 500 m at depth. Table 2 summarizes the relevant physical and numerical model parameters.

The data-assimilative solutions shown below are obtained by utilizing PEZ-HAT configured as a client of the Inverse Ocean Model (IOM). The IOM is a software system that generates a custom variational data-assimilative solver for any functionally smooth ocean model and observing system (Bennett et al., 2008; Muccino et al., 2008). It implements a suite of data-assimilation algorithms and analysis tools with the data structures and algorithms of its client model. We use the combined PEZ-HAT/IOM system to estimate the tidal fields which most nearly agree with the HFR observations and the dynamics of PEZ-HAT, in the sense described below.

2.2.1. Governing equations

When tidal solutions are sought, the core time-dependent primitive equations solver (PEZ) is integrated forward from zero initial conditions until a nearly periodic solution is obtained. This solution is then harmonically analyzed to obtain complex tidal amplitudes for the dependent variables. In general, there may be any number of tidal frequencies present; however, the present work includes

Table 2
PEZ-HAT numerical and physical parameters.

Parameter	Value
Δx (interior)	2 km
Δx (sponge)	20 km
Δz (surface)	30 m
Δz (deep)	500 m
A_V	5×10^{-4} m^2/s
K_V	0.5×10^{-4} m^2/s
A_H, K_H	12 m^2/s
$b_o(z)$	HOTS
$\Delta t'$	50 s
Δt	1.25 s
T	14M_2 periods
T_{HA}	3 M_2 periods

The linearized primitive equations are solved in spherical polar coordinates with approximate horizontal resolution Δx; vertical resolution is Δz. Baroclinic and barotropic time steps are denoted $\Delta t'$ and Δt, respectively. Equations are solved in the time interval $[0, T]$ with harmonic analysis during $[T - T_{HA}, T]$.

only the dominant semidiurnal M_2 tidal frequency, here denoted ω. Let $Re\{\cdot\}$ denote the real part, and assume that the tidal perturbations to the background are given by $Re\{(\mathbf{u}, w, b, \rho, p, \eta)\exp(i\omega t)\}$, where $\mathbf{u}$ denotes the horizontal velocity vector (u, v), w is the vertical velocity, $b = -\rho g/\rho_o$ is buoyancy (computed from potential density ρ), p is the pressure, and η is the elevation of the free surface. The background buoyancy field b_o, which varies only in z, is computed from the HOTS station ALOHA data averaged from September 2002 to May 2003 (Fujieki et al., 2005, 2006). With this notation, the linearized primitive equations, expressed in terms of the complex tidal amplitudes, are

$$i\omega\mathbf{u} + f\mathbf{k}\times\mathbf{u} = -\frac{1}{\rho_o}\nabla p + \mathbf{F} + D^u\mathbf{u} + \hat{\boldsymbol{\upsilon}}, \tag{1}$$

$$-b = -\frac{1}{\rho_o}\partial_z p, \tag{2}$$

$$\nabla\cdot\mathbf{u} + \partial_z w = 0, \tag{3}$$

$$i\omega b + \nabla\cdot(\mathbf{u}b_o) + \partial_z(wb_o) = D^b b + \hat{\beta}, \tag{4}$$

where ρ_o is the constant value of density used in the Boussinesq approximation, $\mathbf{F}$ denotes the tide-generating force, ∂_z is the partial derivative operator with respect to z, and ∇ and $\nabla\cdot$ are the horizontal components of the gradient and divergence operators, respectively. Turbulent mixing is represented with $D^u\mathbf{u}$ and $D^b b$. Coordinate variables are λ, ϕ, and z, longitude, geographic latitude, and height, respectively.

The vector field $\hat{\boldsymbol{\upsilon}} = (\hat{\mu}, \hat{\nu})$ represents forcing in the horizontal momentum equations to account for errors due to the neglect of the nonlinear terms and errors in the mixing parameterization; likewise, $\hat{\beta}$ plays the same role in the buoyancy (mass) conservation equation. Estimates for both $\hat{\boldsymbol{\upsilon}}$ and $\hat{\beta}$ are found in the inversion procedure. They are the smallest forcing corrections necessary to reconcile the model's surface velocity fields with the HFR data, as described in Section 2.2.2.

Turbulent mixing of momentum and buoyancy are parameterized with downgradient transport,

$$D^u\mathbf{u} = \nabla\cdot(A_H\nabla\mathbf{u}) + \partial_z(A_V\partial_z\mathbf{u}), \tag{5}$$

and

$$D^b b = \nabla\cdot(K_H\nabla b) + \partial_z(K_V\partial_z b). \tag{6}$$

PEZ-HAT has been designed to use a Richardson number-dependent scheme to compute the mixing coefficients; however, in this study we have used constant values given by $A_H = K_H = 1.25 \times 10^1$, $A_V =$

5×10^{-4}, and $K_V = 0.5 \times 10^{-4}$ m^2/s. These values yielded stable numerical integrations over the range of resolutions and topographic configurations considered, with damping timescales in excess of 5 tidal cycles for the first internal mode. At the ocean bottom and surface, the normal components of the turbulent fluxes of heat and momentum are zero. For $\mathbf{u}$, we have the free-slip condition in the form

$$A_H \nabla \mathbf{u} \cdot \mathbf{n} = 0 \quad \text{and} \quad A_V \partial_z \mathbf{u} = 0, \tag{7}$$

while buoyancy b obeys

$$K_H \nabla b \cdot \mathbf{n} = 0 \quad \text{and} \quad K_V \partial_z b = 0. \tag{8}$$

PEZ-HAT does include a representation of the stress within the turbulent bottom boundary layer (namely, $A_V \partial_z \mathbf{u} = C_D \mathrm{u}_\star \mathbf{u}$); however, the drag coefficient (C_D) and friction velocity ($\mathrm{u}_\star$) have been set to zero in this study.

Kinematic boundary conditions at material surfaces of the fluid are

$$w + \mathbf{u} \cdot \nabla H = 0, \tag{9}$$

at the ocean bottom, $z = -H(\lambda, \phi)$, and

$$i\omega\eta = w, \tag{10}$$

at $z = 0$. The surface boundary condition on pressure is $p = \rho_0 g \eta$, at $z = 0$.

At open boundaries, the boundary conditions are posed separately for the baroclinic and barotropic components of the flow. Barotropic fields are defined as vertical averages, indicated with the overbar (except for $\bar{w}$, defined below), i.e.,

$$\bar{a} = \frac{1}{H} \int_{-H}^{0} a \, \mathrm{d}z, \tag{11}$$

where the water depth is H. Baroclinic fields are defined as deviations from the barotropic and denoted with a prime, i.e., $a' = a - \bar{a}$. The boundary-normal barotropic flow is set with Dirichlet-type conditions,

$$\bar{\mathbf{u}} \cdot \mathbf{n} = U, \tag{12}$$

where U is the imposed (boundary-normal) barotropic velocity, and $\mathbf{n}$ is the outward normal. A no-stress boundary condition is used for the tangential component of the barotropic velocity. Wave radiation boundary conditions are used for the baroclinic velocity and the active tracer b,

$$i\omega\mathbf{u}' + c_p \nabla \mathbf{u}' \cdot \mathbf{n} = 0, \tag{13}$$

and

$$i\omega b + c_p \nabla b \cdot \mathbf{n} = 0, \tag{14}$$

where the wave speed, c_p, is set to the phase speed for the first internal mode.

2.2.2. Adjoint model

The framework for data-assimilative modeling and analysis in the IOM is based on a least-squares variational formulation of maximum likelihood estimation. If the errors in the model and data are normally distributed with known covariance, the IOM obtains the maximum likelihood estimator for the model's dependent variables. In practice, the structure of the errors is known approximately, at best, and the IOM produces a regularized estimate of the dependent variables. This estimate is the unique set of fields which minimizes a weighted sum of squared data and model residuals (Bennett et al., 2008; Bennett, 2002; Chua and Bennett, 2001). Assuming that the model errors are exclusively in the momentum and mass conservation equations, our estimate for the tidal fields minimizes the cost function,

$$J(\mathbf{u}, w, b, p, \eta) = \hat{\boldsymbol{\upsilon}} \circ \boldsymbol{\upsilon} + \hat{\beta} \circ \beta + (\mathcal{L}[\mathbf{u}] - \mathbf{d})^T \mathbf{C}_{\mathbf{dd}}{}^{-1} (\mathcal{L}[\mathbf{u}] - \mathbf{d}), \tag{15}$$

where $\circ$ denotes the inner product corresponding to integration over the three-dimensional spatial domain, $\mathbf{d}$ is the real-valued vector of observed data, $\mathcal{L}$ is a vector of observation operators that act

on $\mathbf{u}$, and $\mathbf{C_{dd}}$ is the hypothesized measurement error covariance matrix. The weighting of the model errors is implicit in the definitions of β and $\boldsymbol{\upsilon}$, Lagrange multipliers for (1) and (4), namely,

$$\hat{\boldsymbol{\upsilon}} = \boldsymbol{C}_{\upsilon\upsilon} \circ \boldsymbol{\upsilon} \quad \text{and} \quad \hat{\beta} = C_{\beta\beta} \circ \beta, \tag{16}$$

where $\boldsymbol{C}_{\upsilon\upsilon}$ and $C_{\beta\beta}$ are estimates of the spatial covariances of the errors in the momentum and mass conservation equations, respectively, both functions of $(\lambda, \phi, z; \lambda', \phi', z')$. It is tacitly assumed that the data and model forcing errors are uncorrelated.

Minimization of J is accomplished via the indirect representer algorithm of Bennett (2002), originally developed in the context of barotropic tidal estimation (Egbert et al., 1994). For this purpose, the so-called adjoint model must be integrated; these are the equations governing the Lagrange multipliers associated with the minimization of (15) subject to (1)–(14). A lengthly but straightforward application of integration by parts yields,

$$-i\omega\boldsymbol{\upsilon} - f\mathbf{k}\times\boldsymbol{\upsilon} = \nabla\varpi + \Gamma + D^u\boldsymbol{\upsilon}, \tag{17}$$

$$\beta\partial_z b_o = \partial_z\varpi, \tag{18}$$

$$\nabla\cdot\boldsymbol{\upsilon} + \partial_z\pi = 0, \tag{19}$$

$$-i\omega\beta + \pi = D^b\beta; \tag{20}$$

with boundary conditions

$$\boldsymbol{\upsilon}\cdot\mathbf{n} = 0 \quad \text{on open boundaries;} \tag{21}$$

$$\pi + \boldsymbol{\upsilon}\cdot\nabla H = 0 \quad \text{on } z = -H(\lambda,\phi); \text{ and} \tag{22}$$

$$-i\omega\epsilon + g\pi = 0 \quad \text{and} \tag{23}$$

$$\varpi - \epsilon = 0 \quad \text{on } z = 0. \tag{24}$$

Note that the change of variables, $\hat{\mathbf{u}} = \boldsymbol{\upsilon}$, $\hat{p}/\rho_o = -\varpi$, $\hat{b} = \beta\bar{b}_z$, $\hat{w} = \pi$, and $g\hat{\eta} = -\epsilon$ transforms the system (17)–(24) into (1)–(14) with the following modifications to the Coriolis parameter and diffusion operators: $f \to -f$, and $D^b b \to \bar{b}_z D^b(\hat{b}/\bar{b}_z)$. The inhomogeneity, Γ, is a given linear combination of the observation kernels in $\mathcal{L}$.

The implementation utilizing the IOM requires a solver for the forward model, (1)–(14); a solver for the adjoint model, (17)–(24); definition and implementation of the model forcing error integrations, (16); and the definition and implementation of the observation operators $\mathcal{L}$ in Eq. (15) and implicitly in (17). The solver for the forward model was described in Section 2.2; the other implementations are as follows:

The adjoint solver for Eqs. (17)–(24) is implemented with the finite-difference of the continuous adjoint equations (Sirkis and Tziperman, 1997). The accuracy of the adjoint properties of the system were verified by conducting a series of convergence experiments as the grid- and temporal resolution of the solver was increased. Errors in the adjoint properties are due primarily to the spin-up and harmonic analysis procedures in PEZ-HAT. Using the model grid and time-stepping parameters in Table 2, symmetry errors in the adjoint solver are between 10 and 20%.

The model forcing error covariance integrations (Eq. (16)) are implemented via a factorization of the form $C = (C^{1/2})^\dagger C^{1/2}$, where

$$C^{1/2}(\lambda,\phi,z;\lambda',\phi',z') = \prod_{p=1}^{P} c_\lambda(\lambda,\lambda')c_\phi(\phi,\phi')c_z(z,z')\sigma(\lambda',\phi',z'), \tag{25}$$

and the uni-dimensional kernels (c_λ, c_ϕ, c_z) are solutions of

$$\left(1 - L_x^2\frac{\partial^2}{\partial x^2}\right)c_x = \mathcal{N}_x\delta(x - x'), \tag{26}$$

where $\delta(x)$ is a Dirac delta function and $\mathcal{N}_x$ is a normalization coefficient, the † denotes operator adjoint, and $x \in \{\lambda, \phi, z\}$. Neumann boundary conditions are used. The parameters L_x and P are selected to yield

the desired spatial correlation scale and asymptotic power-spectrum roll-off rate of the respective model forcing errors, $\boldsymbol{C}_{\boldsymbol{\nu\nu}}$ and $C_{\beta\beta}$. The parameter σ is the nominal amplitude of the forcing error. Normalization coefficients, $\mathcal{N}_x$, are obtained from the requirement that $C(\lambda, \phi, z; \lambda, \phi, z) = \sigma^2(\lambda, \phi, z)$. The rationale behind the formulation (25) is that the inner products in (16) are computed with fast tridiagonal solvers for the uni-dimensional systems (26). Another consequence is that the normalization coefficients can be determined exactly on a uniform grid. This implementation can be regarded as a generalization of the approach in Purser et al. (2003), where the convolutions are implemented with spatially lagged recursive filters. The models (25) and (26) are an approximation to the radially symmetric covariance functions proposed by Whittle (1954), later generalized and analyzed in Vecchia (1985).

The observation operators $\mathcal{L} = \{\ell_m\}_{m=1}^{M}$ are parameterized by the location (λ_m, ϕ_m) and the azimuthal angle (Φ_m) towards the HFR array at each point in the antenna's field of view, i.e.,

$$\ell_m[\mathbf{u}] = u(\lambda_m, \phi_m, 0) \cos \Phi_m + v(\lambda_m, \phi_m, 0) \sin \Phi_m. \tag{27}$$

The implementation follows from expressing ℓ_m as linear operator on $\mathbf{u}$,

$$\ell_m[\mathbf{u}] = \mathbf{L}_m(\lambda, \phi, z) \circ \mathbf{u}, \tag{28}$$

with

$$\mathbf{L}_m = \delta(\lambda - \lambda_m, \phi - \phi_m, z) \begin{pmatrix} \cos \Phi_m & 0 \\ 0 & \sin \Phi_m \end{pmatrix} \tag{29}$$

and $\delta(\lambda, \phi, z)$ is the Dirac delta function in spherical-polar coordinates.

2.3. Hypothesized model errors, $\boldsymbol{C}_{\boldsymbol{\nu\nu}}$ and $C_{\beta\beta}$

In this section we analyze the errors, both physical and numerical, in PEZ-HAT in order to justify the weights used in the cost function (15).

Errors in the forcing functions, boundary conditions, and bottom topography. The astronomical forcing functions and boundary conditions on the barotropic flow are known with great accuracy. The principle errors in the astronomical forcing are connected with uncertainty in the treatment of solid-earth loading and self-attraction. These are on the order of 5% of the astronomical potential (Egbert et al., 2004), which, while significant, is largely in equilibrium with the tidal solution forced by the barotropic boundary conditions. The barotropic open boundary currents are taken from a highly accurate regional data-assimilative model which is constrained by satellite altimetry data and the best available global tidal solutions (Zaron and Egbert, 2006a). The barotropic currents are believed to be accurate within a few 1 cm/s (Zaron and Egbert, 2007; Dushaw et al., 1997).

Because the site of the HFR observations is dominated by a locally produced baroclinic tide we neglect errors connected with the baroclinic open boundary condition and sponge layer. In other words, we assume that the remotely generated internal tide which propagates into the domain is negligible.

Of more significance are potential errors in the bottom boundary conditions due to uncertain bathymetry. The consequences of these errors can be understood from the analysis of Llewellyn Smith and Young (2002), who derived the energy conversion rate for a barotropic tidal current over small amplitude topography. Utilizing the Green's function for the primitive equations (linearized around a state of uniform stratification and small-amplitude topography), they find that the baroclinic pressure field is proportional to ∇h, and the energy flux is proportional to $|\mathbf{k}||\tilde{h}(\mathbf{k})|^2$, where $|\tilde{h}(\mathbf{k})|^2$ is the power spectral density of the topography, a function of the two-dimensional wavenumber, $\mathbf{k} = (k, l)$. This spectral representation shows that the internal tidal fields are sensitive to the high-wavenumber components of the bathymetry (cf., Zaron and Egbert, 2006a).

The bathymetric data used are a compilation of multi-beam sonar smoothed and gridded at 2 km resolution (Carter, 2006). Comparison with another high-resolution bathymetric database (150 m-resolution, Eakins et al., 2003) indicates that the largest errors are inhomogenously distributed, with root-mean-square errors of 45 m, but median absolute errors of only 12 m. Below 500 m depth, the

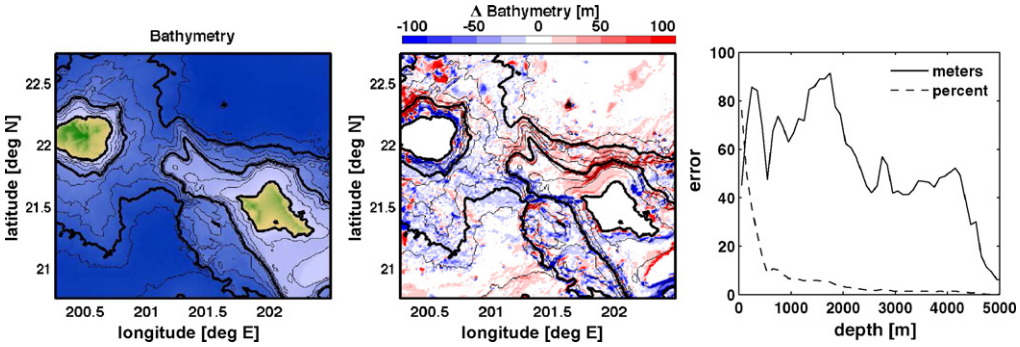

Fig. 2. Bathymetric uncertainty. Left: 2 km-resolution bathymetry (thick contours every 2000 m; thin contours every 500 m). Center: difference, 2 km- vs. 150 m-resolution bathymetry data, smoothed and gridded to 2 km. Contours lines are the same as in left panel. Right: root-mean-square depth difference, binned in 50 m depth intervals.

root-mean-square errors are uniformly less than 10%, and below 2000 m the errors are less than 5%. The 1 km-resolution bathymetry and statistics of the comparison with 150 m-resolution data are shown in Fig. 2.

Errors in the physics of PEZ-HAT. The hydrostatic and Boussinesq approximations are the primary physical approximations in the primitive equations. Both of these are very satisfactory at the scale and resolution of our modeling efforts. Additionally, we have adopted the "traditional approximation" of the Coriolis force which is justified in the upper ocean where N^2/f^2 is large (Gerkema, 2006).

Of more significance is the error connected with the linearization of the primitive equations around a horizontally uniform background state. The neglected terms are $u \cdot \nabla u$ in Eq. (1) and $u \cdot \nabla b$ in Eq. (4). We hypothesize that these terms are dominated by the components due to steady or slowly varying non-uniform background state. We take $\tilde{u}_0 = 0.2$ m/s as a typical speed for the surface mesoscale currents (Chavanne et al., submitted for publication-a, s), decaying vertically like $N^{1/2}$, with a horizontal correlation scale of $L = 25$ km and a vertical correlation scale of 300 m. The spatial correlations are assumed to asymptote to -4 power dependence for large wave number, which insures spatial regularity for the linearized primitive equations. Using the prior, data-less, solution, we estimate $u_0 = 0.25$ m/s as the scale for the tidal surface velocity, and assume the same horizontal and vertical scaling as the mesoscale field. The same basic scaling is also applied to the mass equation (4) using a buoyancy scale b_0 equivalent to a tidal temperature perturbation of 6 °C at the depth of the $N_o^2 = -(b_o)_z$ maximum. In summary, we assume

$$\sigma_{\boldsymbol{v}}(z) = \frac{\tilde{u}_0 u_0}{L}\frac{N_o(z)}{\bar{N}} \quad \text{and} \quad \sigma_\beta(z) = \frac{\tilde{u}_0 b_0}{L}\frac{N_o(z)}{\bar{N}}, \tag{30}$$

where $\bar{N}$ is the vertical average of N_o.

Error caused by our simplified representation of the Reynolds stress is more difficult to estimate. The HOME project found that turbulence dissipation is largest within 60 km of the Hawaiian Ridge axis, with significant variability in space and time, which is not independent of the tides (Klymak et al., 2006; Rudnick et al., 2003). Rather than make any attempt to realistically model the turbulent cascade in PEZ-HAT, we have taken the approach of minimizing the explicit impact of the Reynolds stresses by assuming downgradient turbulence transport and small, spatially constant, transport coefficients. A posteriori, we can check the validity of this approach by estimating upper bounds on the size of the Reynolds stress divergence in comparison with the diagnosed tidal-mesoscale and tidal self-interactions. This is done in Section 3, below, and we find that the impact of turbulence transports on the tidal fields is likely to be minimal, except in boundary layers at the ocean surface and bottom.

Numerical solver errors. The numerical truncation errors in PEZ-HAT may be significant, and depend largely on how well the bathymetric features are resolved. For two-dimensional experiments, the empirical order of convergence for PEZ-HAT is quadratic in the model's prognostic variables, which leads to essentially linear convergence of energetic diagnostics (Zaron and Egbert, 2006a). Comparisons

of PEZ-HAT with analytical solutions for the tidal conversion over a two-dimensional ridge (Petrelis et al., 2006) indicate that resolution of 5 km in the horizontal and 80 m in the vertical is necessary to resolve the barotropic to baroclinic energy conversion to within 10% for smooth ridge profiles similar to Ka'ena Ridge (Zaron and Egbert, 2006b). Precise convergence criteria in three dimensions for realistic topography are not known, but the requirements are evidently stringent (Carter et al., 2008; Simmons et al., 2004a; Niwa and Hibiya, 2004). In the present application, convergence experiments suggest that the truncation errors are comparable to the uncertainty caused by the bathymetric data, being roughly 5% to 10%.

3. Results

3.1. Data-less prior solution

The prior model is governed by the primitive equations, described above, and it is forced via barotropic tidal currents inferred from a larger-scale data-assimilating barotropic tidal model (Zaron and Egbert, 2006a). The boundary forcing is consistent with the full record of TOPEX/Poseidon altimetric data, from which we infer that the surface tide loses energy at a rate of 1.1–1.7 GW in Kauai Channel and the nearby region. This value is uncertain for the small domain considered here, given the nominal inter-track spacing of 200 km (Zaron and Egbert, 2006a). However, the use of a prescribed barotropic velocity boundary condition in PEZ-HAT does not constrain the value of the barotropic energy loss, because this quantity is determined by the relative phase of the barotropic transport and the ocean surface elevation on the boundary (Egbert and Ray, 2000), and this latter quantity is free to adjust in these simulations.

Fig. 3 illustrates the solution of the prior model, and the reader is referred to (Chavanne et al., submitted for publication-a) for a more detailed comparisons to the HFR as well as other model simulations. The elevation of the free surface is dominated by the barotropic tide (Fig. 3 A, shown at the time of maximum across-ridge gradient), with small perturbations from the internal tide. The dynamic height anomaly, i.e., $\int_{-H}^{0} b\,\mathrm{d}z$ (Fig. 3B), shows more clearly the amplitude and phase propagation of the low-mode internal tide generated at Ka'ena Ridge. Section views, looking to the northwest along the ridge (Fig. 3 D and E), show intensification of tidal kinetic energy along characteristics of the internal tide, and isopycnal displacements in excess of 50 m. The beams of elevated kinetic energy intersect the ocean surface approximately 40 km from the ridge, where they are associated with enhanced surface kinetic energy (Fig. 3C). The intensification of kinetic energy along tidal characteristics is the result of coherent propagation of multiple wave modes. Kinetic energy is elevated because the energy density of the ray tubes is proportional to the surface area of their intersection with the bottom.

For comparison with the HFR observations, Fig. 4 shows the radial component of the M_2 surface velocity field computed with PEZ-HAT. The model has a well-defined band of high velocity south of Keana ridge, at 21.5°N, which is associated with the first surface bounce of the internal tide generated on the north side of the ridge (Nash et al., 2006). Compared to the HFR data (cf., Fig. 1), the surface radial velocities and their spatial gradients are larger in the model. While there is some qualitative similarity between the model and observations, the differences are, on average, about twelve times larger than the data uncertainty (right panel, Fig. 1). Can these differences be explained by tidal-mesoscale interactions? We address this question next, by generalized inversion of the primitive equations together with the HFR data.

3.2. Data-assimilative solutions

The methodology described in Section 2 has been used to assimilate data from the two periods, P1 and P2, into PEZ-HAT. For each period we obtain an estimate of the tidal fields that minimize the weighted sum of squared model and data errors (15), where the observations are weighted with the inverse of the nominal observation error, and the model dynamics are weighted with the inverse of a plausible estimate of the model forcing error. Because the estimated tidal fields do not exactly satisfy the equations of motion, we also obtain estimates of the advective and convective terms which are

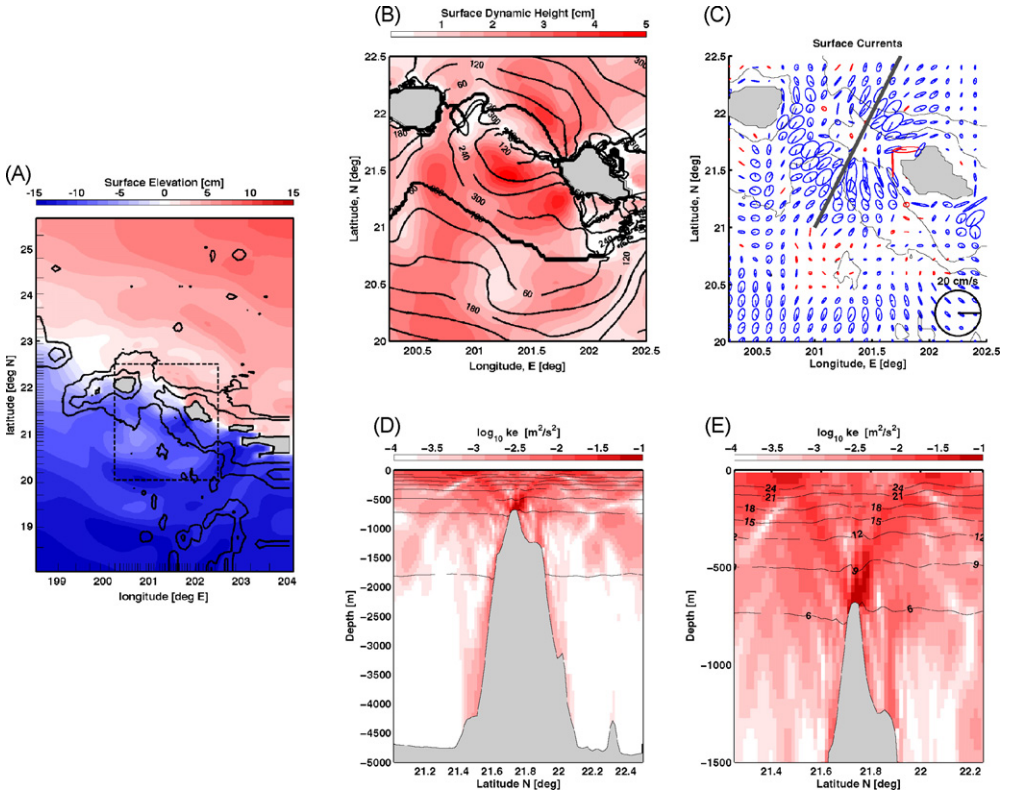

Fig. 3. Prior solution. (A) Surface elevation: the domain of the numerical model is shown together with the 0, 2000, and 4000 m isobaths. Tick marks along the south and west border of the plot show every third model grid point. The color scale shows the surface elevation at the time of the maximum across-ridge gradient. The dashed line indicates the subdomain which is shown in subsequent figures. (B) Surface dynamic height: the phase (degrees) and amplitude (cm) of the surface dynamic topography is shown. (C) Surface currents: tidal ellipses for the nominal surface currents are shown. Color indicates clockwise (red) or counterclockwise (blue) rotation of the current vectors. The gray line indicates the position of the sections shown in (D) and (E). (D) $\log_{10}ke$: log-scaled kinetic energy is shown across the ridge. The solid lines are isotherms from 3 to 21 °C. (E) $\log_{10}ke$: The section in (D) is enlarged to show the crest of the ridge. Isotherms are labeled. (For interpretation of the references to color in this figure legend, the reader is referred to the web version of the article.)

hypothesized to be the dominant source of error in the model. These terms will be referred to as the model residuals.

Fig. 5 shows the difference fields for the optimal estimates of the radial velocity for P1 and P2. The estimated velocity fields, not shown, are visually indistinguishable from the observations in Fig. 1. The model-data residual tends to increase with increasing range from the antennas, in accordance with the expected errors. This is further illustrated in Fig. 6, which shows the probability density of the model-data residual during P1. On average, the residual in the optimal solution is about 2/3 the nominal data error. The number of observations in the P1 assimilation is $M = 5694$. The residual is not Gaussian and the data assimilative solution appears to over-fit most of the data (there are too many small deviations relative to a Gaussian with the same variance). Thus, there may be some benefit to refining the model and data error estimates; however, it appears that they are estimated to within better than an order of magnitude. The distribution of misfits for the P2 assimilation ($M = 5058$) is similar (not shown).

Figs. 7 and 8 show other views of the data-assimilative solutions during P1 and P2. Compared with the prior solution (Fig. 3), we can see that the surface dynamic height (panel B), i.e., the surface expression of the internal waves, exhibits a complicated pattern of phase propagation from the ridge. The amphidrome south of O'ahu in the prior evidently depends on a rather delicate balance of local and

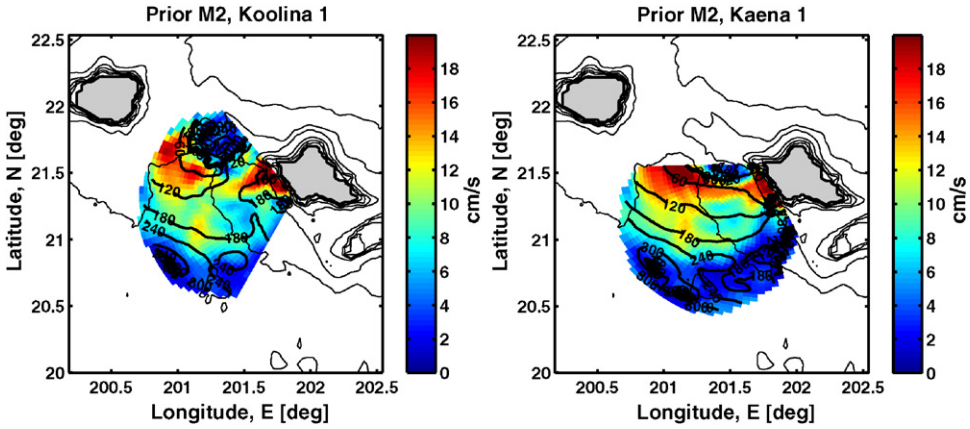

Fig. 4. Prior solution: radial velocity. The amplitude (cm/s) and phase (degrees) of the surface radial velocity is shown with respect to Ko'Olina (left) and Ka'ena Point (right).

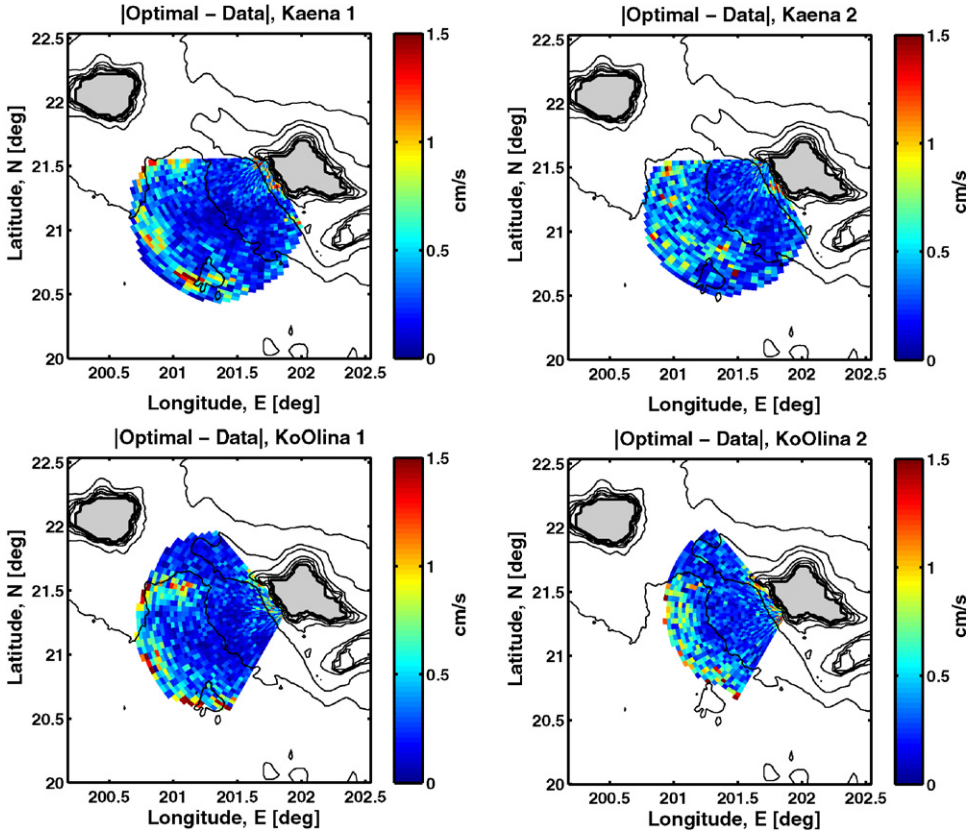

Fig. 5. Model-data residual. The panels show the absolute value of the model-data residual in the data-assimilative solutions for P1 (left panels) and P2 (right panels). The M_2 radial velocities in the data assimilative solutions are visually indistinguishable from observations in Fig. 1.

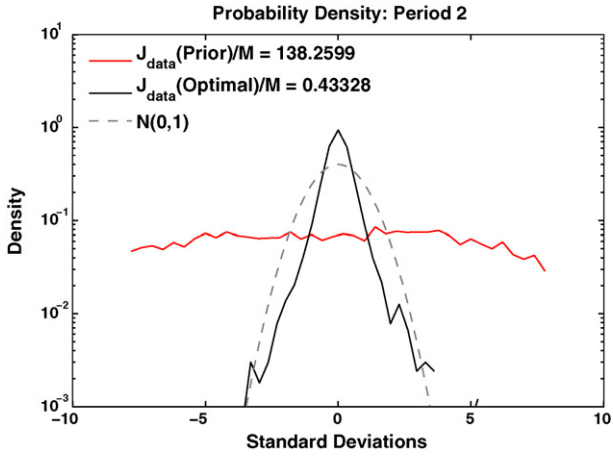

Fig. 6. Distribution of data residuals. The probability distribution of the model-data residual during P2 is shown, where the residual has been normalized by the nominal data error. The mean residual for the prior solution (red line) is, on average, $(138)^{1/2} \approx 12$ times larger than the nominal data error. The mean residual for the optimal solution (solid black line) is, on average, $(0.433)^{1/2} \approx 2/3$ the nominal data error. Comparison with the normalized Gaussian (dashed gray line) shows that the misfit of the optimal solution is not normally distributed. (For interpretation of the references to color in this figure legend, the reader is referred to the web version of the article.)

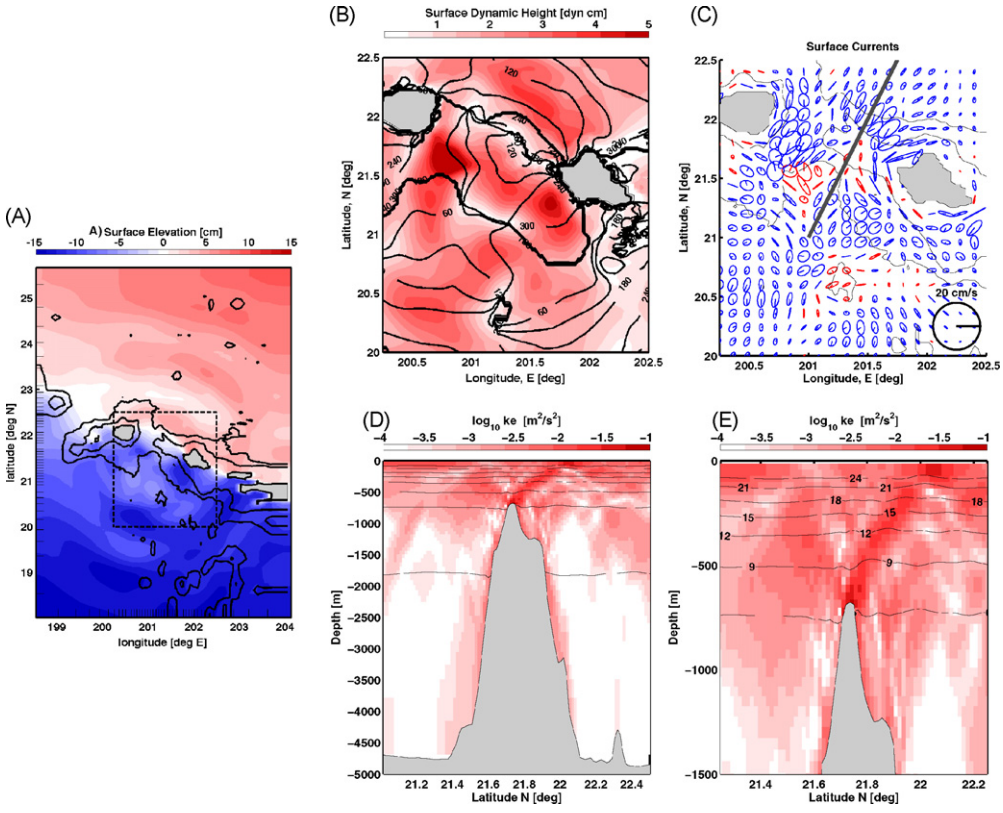

Fig. 7. P1 solution. The optimal solution during P1 is shown. Panels are as in Fig. 3.

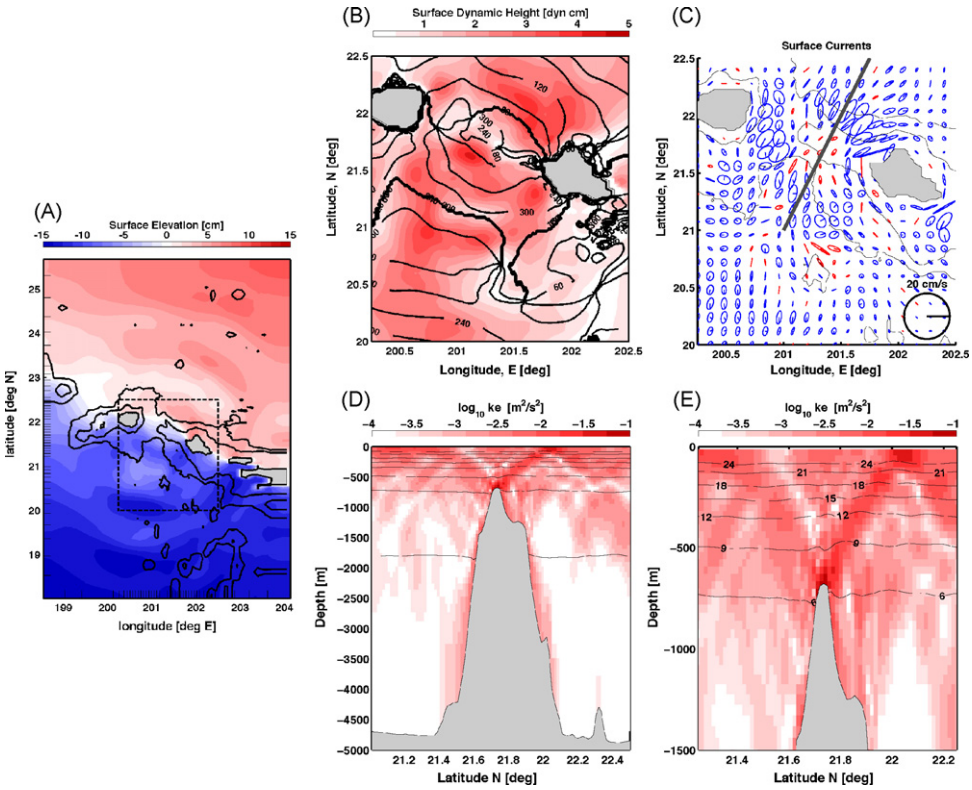

Fig. 8. P2 solution. The optimal solution during P2 is shown. Panels are as in Fig. 3.

remotely generated waves for its existence. During P1, the surface velocities (panel C) are intensified at the western most extent of the Ko'Olina array viewing area, about 20 km southeast of Kauai. This feature is not present during P2. The cross-sectional views (panels D and E) show that the southward beam of baroclinic energy has been diminished, while the northward beam has been intensified. Although these features appear as beams, they are actually sheets of elevated kinetic energy in three dimensions. It is unfortunate that data north of the ridge is lacking, as it would provide some validation of those aspects of the data assimilative solutions which are removed from the HFR observing arrays.

3.3. Comparison with independent data

Figs. 5 and 6 indicate that the data assimilative solutions are plausible when judged solely against the HFR data. However, some aspects of the solution appear to be less plausible, such as the surface-intensified currents southeast of Kauai during P1. To assess the validity of the data assimilative solutions, we utilize two other sources of information, namely, (1) moored acoustic Doppler current profilers (ADCP) from the Hawai'i Ocean Mixing Experiment (HOME), and (2) satellite altimetry.

Fig. 9 compares the optimized solution during P2 with data from the HOME A2 mooring (the reader is referred to Chavanne et al., submitted for publication-a and Zilberman et al., 2008 for details regarding the moorings). The amplitude of the currents is improved in the upper 400 m of the water column, and the phase is changed slightly. This mooring is located on the flank of Ka'ena Ridge, near its southwest edge, in water approximately 1300 m deep. One can see that the mismatch in the currents below 1000 m are not improved in the assimilative solution. These unrealistic bottom currents in the model are responsible for a beam of baroclinic energy that intersects the ocean surface north of the ridge.

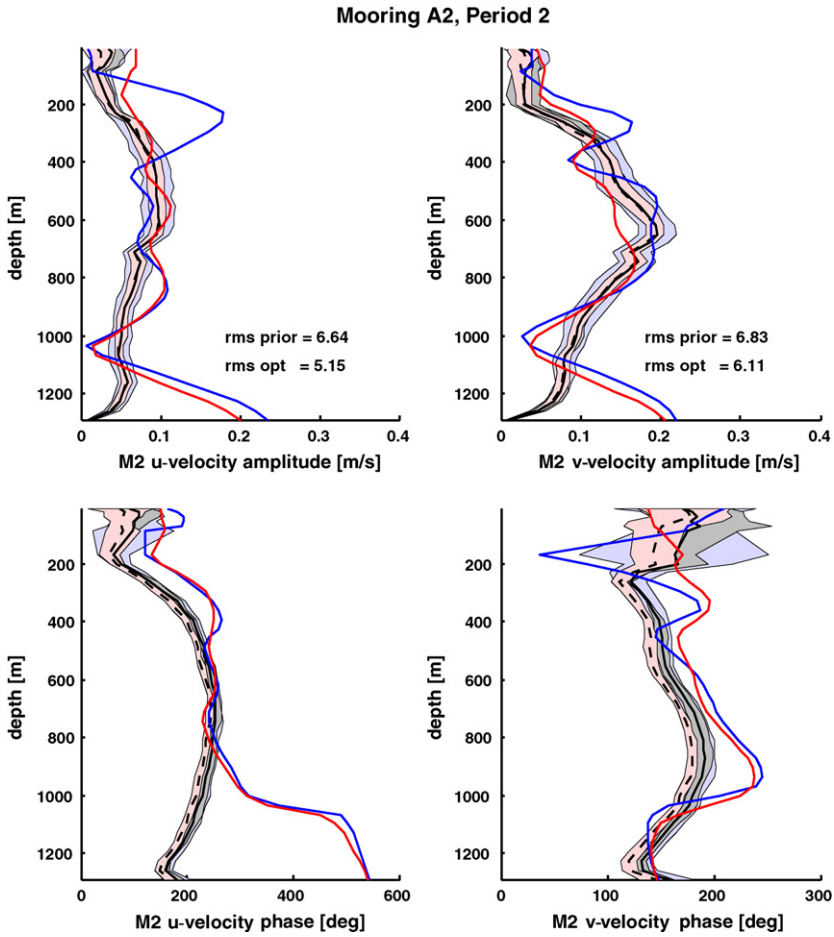

Fig. 9. Comparison with A2 mooring. The panels show the PEZ-HAT prior (blue line), P2 optimal solution (red line), and mooring data (solid black line, harmonic analysis over P2). The dashed black line indicates average values obtained by harmonic analysis over independent 16-day intervals in P2, and the shaded regions show different estimates of the 95% confidence intervals for the mooring data. Root-mean-square errors in the velocity components are given in units of cm/s.

Without observations to the north, there is no way for the data assimilative solution to correct the bottom currents at the site of the A2 mooring. Comparisons at the C1 and C2 moorings (not shown) indicate substantially similar results: root-mean-square misfits are for current amplitudes are reduced by 2–4 cm/s in the upper 400 m. Deeper currents are not significantly altered in the data-assimilative solutions, and, in any event, there is much better agreement at depth at these two sites.

Fig. 10 compares the amplitude and phase of the prior model with satellite altimetry data. The quantitative comparison in each panel (Δrms) is the root-mean-square error over a rectangular area somewhat larger than the HFR viewing area; it is shown only for those satellite ground tracks passing through the HFR viewing area. Because the orbit repeat time and length of time series of TOPEX/Poseidon (TP, 332 orbit cycles), Geosat Follow-On (GFO, 87 orbit cycles), and Earth Remote Sensing (ERS, 47 orbit cycles) all differ (Andersen and Knudsen, 1997), the standard errors for the M_2 amplitude estimates are approximately 1, 1.5, and 2 cm, respectively. The comparisons show that, overall, the model tends to predict a somewhat smaller baroclinic response at M_2 than is present in the data; although, there are significant exceptions and possible anomalies (e.g., GFO-017, ERS-396). Also, there appears to be a systematic offset of approximately 5 degrees in phase north of the Hawaiian

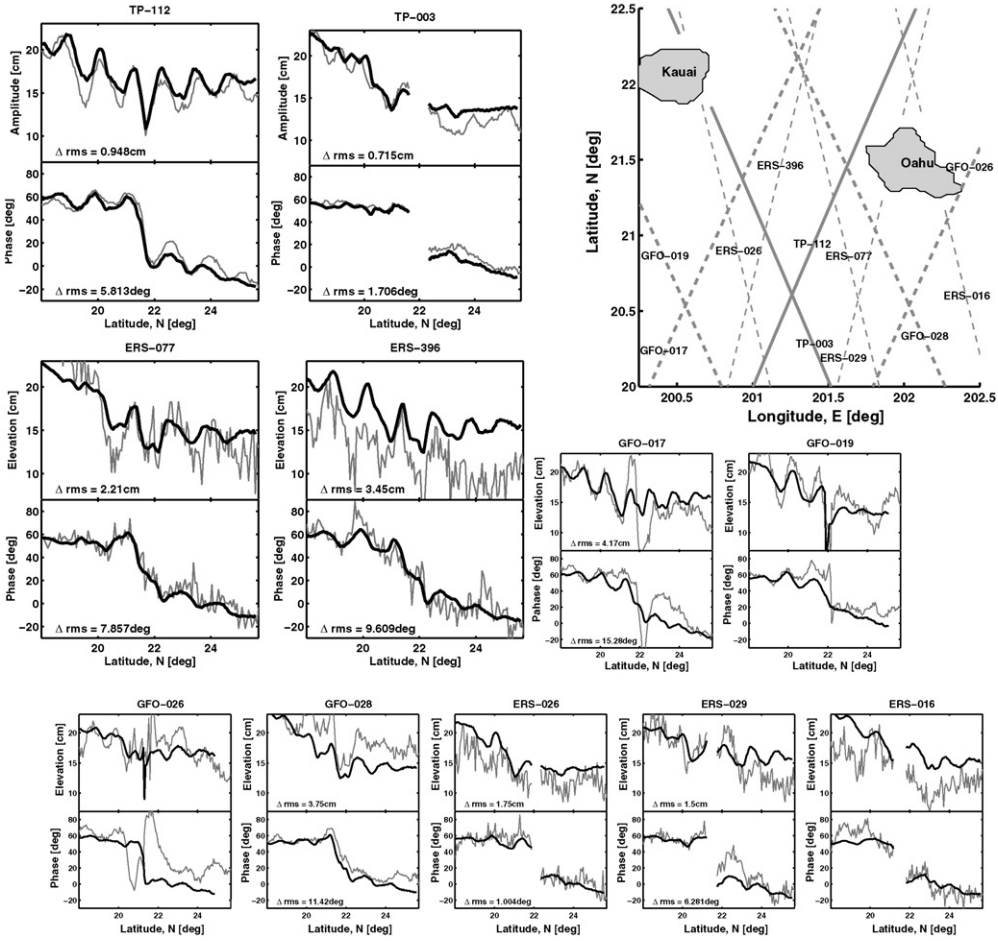

Fig. 10. Satellite data vs. PEZ-HAT prior. Upper-right panel shows satellite ground tracks: TOPEX/POSEIDON (TP, solid line), Geosat Follow-On (GFO, dashed line), and Earth Remote Sensing (ERS, thin dashed line). The other panels show the amplitude and phase of the M_2 harmonic constants for the satellite data (gray line) and the prior solution of PEZ-HAT (dark line).

ridge, with the observed phase leading the model. Again, there are exceptions, ERS-016 and ERS-026, with little or no phase difference.

Of these satellite altimeters, TP has been most widely used in tidal studies, and the differences between the model and TP may reflect either systematic inaccuracies on the model simulation, or they may result from real temporal variability of the tide (cf., Chiswell, 2006). The 10-day repeat time of TP orbit means that it will systematically underestimate the amplitude of the M_2 harmonic constant. Rainville and Pinkel (2006) quantified this for tidal waves refracted by the mesoscale eddy field in the open ocean around Hawai'i, finding the average amplitude of M_2 reduced as much as 0.5 cm within 250 km of the ridge. This number depends greatly on vertical structure of the mesoscale and the detailed modal structure of the tide, with mode-2 and higher impacted much more than the barotropic and mode-1 signals (Chavanne et al., submitted for publication-b).

Comparing the data-assimilative solutions with the satellite altimetry yields equivocal results. There is a 0.2 cm increase in agreement of amplitudes along the TP-112 track for the P1 solution; however, there is a slight decrease in agreement of phase. As shown in Figs. 11 and 12, the data-assimilative surface elevations are only slightly modified from those obtained with the prior model.

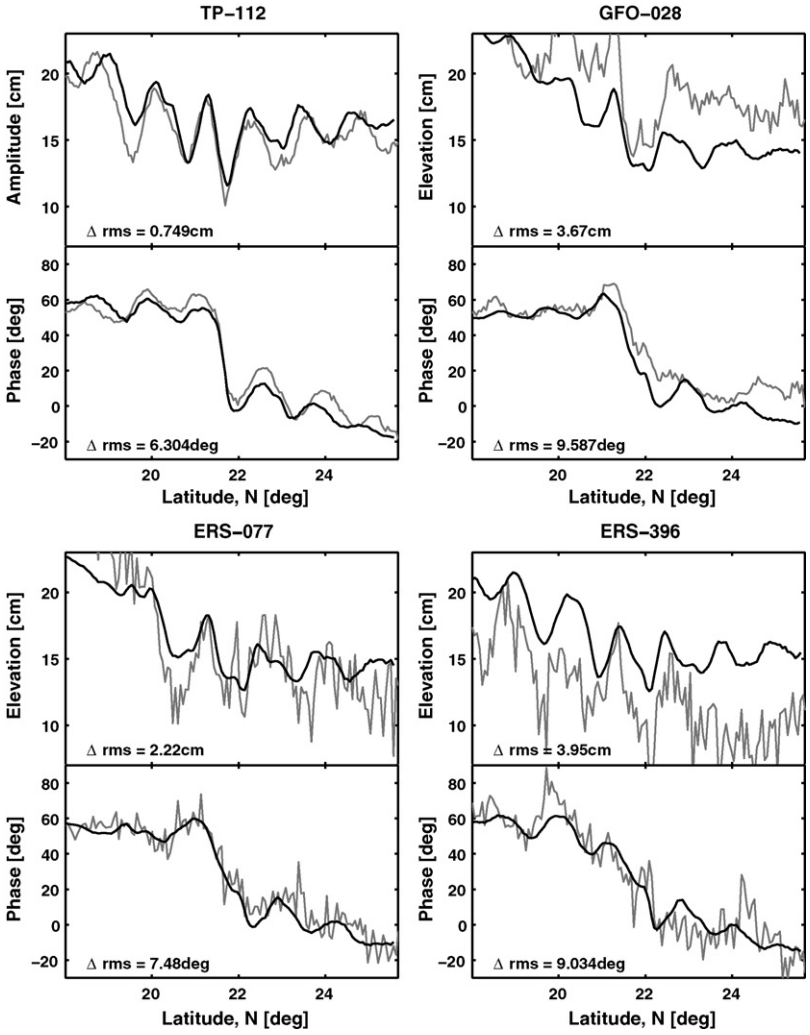

Fig. 11. Satellite data vs. P1 inversion. The altimetry data is compared with the P1 data-assimilative solution along a subset of the ground tracks shown in Fig. 10 that pass through the HFR viewing area. There is a modest improvement in the agreement with the TP-112 track with amplitude errors reduced from 0.95 cm to 0.75 cm, but the phase error is increased from 5.8° to 6.3°. None of the changes in misfit is significant compared to he uncertainty in the altimetry data.

3.4. Residual forcing

The data assimilative solutions provide two sets of quantities, (1) the tidal velocity, buoyancy, and pressure fields, and (2) the residual forcing functions $\hat{\boldsymbol{\upsilon}}$ and $\hat{\beta}$. By construction, the residual forcing is the smallest correction (as measured by the norm implied by the penalty function) which is necessary to bring the modeled surface currents into agreement with the HFR data. In this section, we look at the residual fields to understand the dynamics of the optimal solution, and to evaluate the plausibility of the term balances.

The residual forcing fields are generally largest near the ocean surface, and small compared to the acceleration ($i\omega\mathbf{u}$). How do they compare with the prior estimates? The magnitude of the model residual is shown in Fig. 13 at a series of representative sites for the P1 solution. The diagrams also

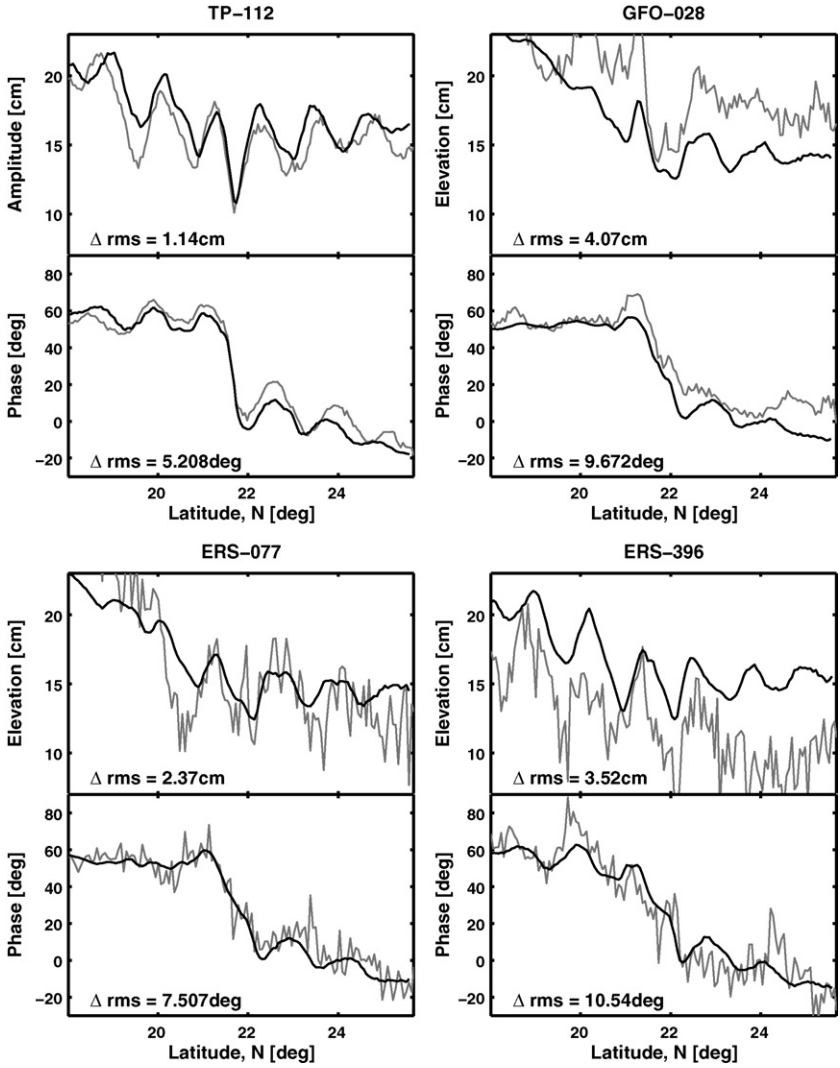

Fig. 12. Satellite data vs. P2 inversion. The P2 data-assimilative solution has somewhat larger misfits, compared to the altimetry data. Like the P1 solution, the changes from the prior solution are smaller than the uncertainty in the altimetry data.

show the nominal prior estimate of the model residual, i.e., $\sigma_{v(z)}$, which was estimated from a scale argument (Section 2.3). Throughout most of the water column (e.g., Site 1), the optimal residual forcing is a factor of ten or more smaller than its hypothesized value, and the corrections to the model are mostly confined to the surface, near the HFR measurements. Over topography that is steep, shallow, or both, the residual forcing is more comparable to its hypothesized magnitude. Overall, the model residual is smaller than its prior estimate, which is consistent with the fact that the data-assimilative solutions over-fit the observations. Results for P2 (not shown) are similar.

A more detailed look at the forcing residuals for P1 is shown in Fig. 14. Once again we see (Fig. 14A) that the forcing corrections are largest within the viewing area of the HFR, although values as high as $0.5\omega|\mathbf{u}|$ occur at the western-most boundary of the viewing area. The other panels in the figure show cross-sections of $|\hat{\boldsymbol{v}}|$ through this surface feature. Panels B and C show a maximum in surface dynamic height and kinetic energy centered near this same site, at the western-most limit of the

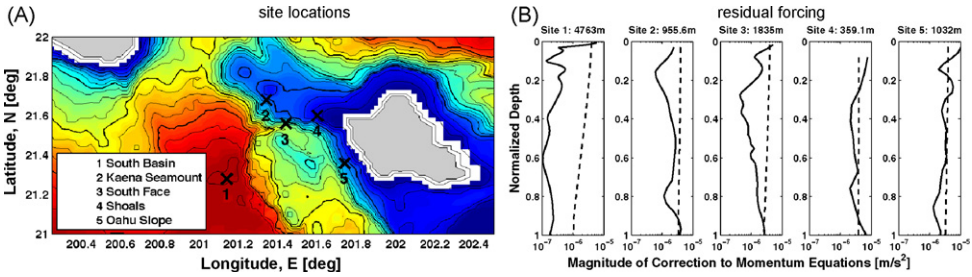

Fig. 13. Model residual forcing. The magnitude of the momentum equation residual forcing, $(|\hat{\mu}|^2 + |\hat{v}|^2)^{1/2}$, is shown at five representative sites. (A) Left: locations of the sites. (B) Right: magnitude of the model residual (solid), and the hypothesized model forcing error (dashed).

observations. Unfortunately, we do not have independent data to evaluate the validity of this region of surface intensified tidal currents. Given its scale and proximity to the edge of the observing array, it should be regarded with caution, but it is noteworthy that a strong mesoscale eddy did pass this edge of the array during P1 (Chavanne et al., submitted for publication-b). In this case the forcing residual is localized to the change in circulation, whereas, in other cases the change in circulation is more related to remote forcing near the topography, or to more subtle changes in modal composition of the fields.

Looking next at the residual forcing in the buoyancy equation, $\hat{\beta}$, we find that it is essentially zero. On average, it is about 10^2 times smaller than the prior estimate, σ_β. The data assimilative solution has the smallest forcing corrections necessary to explain the HFR observations, and corrections to mass conservation are simply unnecessary given the permitted level of error in the momentum equations. This result is a consequence of the rudimentary statistical model for tidal-mesoscale interactions in Section 2.3. A proper representation would involve a state-dependent covariance and would include a proper cross-covariance for β and $\boldsymbol{v}$. A possibly simpler and more expedient approach would involve using a nonlinear model of both the tides and mesoscale; this will be addressed further in Section 4, below.

3.5. Energetics and baroclinic conversion

An examination of the term balance in the equations for kinetic energy and available potential energy is presented in Tables 3 and 4. Because the barotropic and baroclinic velocity fields are orthogonal, by definition, equations for the kinetic energy in each mode are de-coupled in the linearized

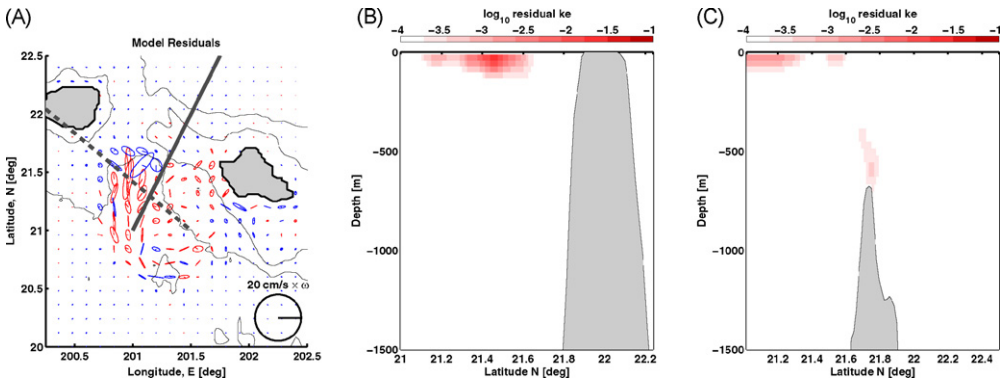

Fig. 14. P1 model residual. (A) Left: scaled residual forcing at the ocean surface, $\omega^{-1}\hat{\boldsymbol{v}}$, units of cm/s (cf., Fig. 3C). Dashed and solid lines indicate cross-sections shown panels B and C, respectively. (B) Middle: scaled residual forcing magnitude, $\omega^{-2}|\hat{\boldsymbol{v}}|^2$, along the dashed section. (C) Right: scaled residual magnitude along the solid section.

Table 3
Energy equation: volume integrals.

Term [units]	Prior	P1	P2
$\|\bar{\mathbf{u}}\|^2$ [TJ]	181	190	167
$-\bar{\mathbf{u}} \cdot \frac{\nabla p^*}{\rho_o}$ [GW]	−0.26	−0.40	−0.25
$\bar{\mathbf{u}} \cdot \mathbf{F}^*$ [GW]	0.45	0.45	0.45
$\bar{\mathbf{u}} \cdot D^u \mathbf{u}^*$ [GW]	−0.14	−0.12	−0.11
$\bar{\mathbf{u}} \cdot \hat{\boldsymbol{\upsilon}}^*$ [GW]	0	0.21	0.05
$\bar{\epsilon}$ [GW]	−0.15	−0.14	−0.14
$\|\mathbf{u}'\|^2$ [TJ]	95.5	105	82.2
$-\mathbf{u}' \cdot \frac{\nabla p^*}{\rho_o}$ [GW]	0.25	0.00	0.12
$\mathbf{u}' \cdot D^u \mathbf{u}^*$ [GW]	−0.13	−0.12	−0.11
$\mathbf{u}' \cdot \hat{\boldsymbol{\upsilon}}^*$ [GW]	0	0.24	0.09
ϵ' [GW]	−0.12	−0.12	−0.10
$\frac{\|b\|^2}{(b_o)_z}$ [TJ]	79.0	88.3	67.4
$-b\bar{w}^*$ [GW]	1.46	1.11	1.22
$-b(w')^*$ [GW]	−1.32	−0.98	−1.10
$\frac{b}{(b_o)_z} D^b b^*$ [GW]	−0.09	−0.08	−0.07
$\frac{b}{(b_o)_z} \hat{\beta}$ [GW]	0	0.00	0.00
ϵ^{APE} [GW]	−0.05	−0.05	−0.05

model. The barotropic kinetic energy equation is

$$i\omega|\bar{\mathbf{u}}|^2 = -\bar{\mathbf{u}} \cdot \frac{\nabla p^*}{\rho_o} + \bar{\mathbf{u}} \cdot \mathbf{F}^* + \bar{\mathbf{u}} \cdot D^u \mathbf{u}^* + \bar{\mathbf{u}} \cdot \hat{\boldsymbol{\upsilon}}^* + \bar{\epsilon}, \tag{31}$$

where super-script* indicates complex-conjugate. Note that Eq. (31) contains an extra term, $\bar{\epsilon}$, which arises because the time-stepping and harmonic analysis procedure in PEZ-HAT does not exactly solve Eq. (1) in the frequency domain. The baroclinic kinetic energy equation is similar,

$$i\omega|\mathbf{u}'|^2 = -\mathbf{u}' \cdot \frac{\nabla p^*}{\rho_o} + \mathbf{u}' \cdot \mathbf{F}^* + \mathbf{u}' \cdot D^u \mathbf{u}^* + \mathbf{u}' \cdot \hat{\boldsymbol{\upsilon}}^* + \epsilon', \tag{32}$$

where we note that $\mathbf{u}' = \mathbf{u} - \bar{\mathbf{u}}$ is orthogonal to $\bar{\mathbf{u}}$. The available potential energy equation is

$$i\omega \frac{|b|^2}{(b_o)_z} = -bw^* + \frac{b}{(b_o)_z} D^b b^* + \frac{b}{(b_o)_z} \hat{\beta} + \epsilon^{\mathrm{APE}}. \tag{33}$$

Because the fluid is incompressible and in hydrostatic balance, integration by parts can be used to show that the energy equations are coupled through the pressure gradient terms,

$$\int_{\mathcal{D}} \mathbf{u} \cdot \nabla p^* + \int_{\mathcal{D}} bw^* = \int_{\partial\mathcal{D}} (\mathbf{u}p^*) \cdot \mathbf{n}, \tag{34}$$

where $\mathcal{D}$ and $\partial\mathcal{D}$ refer to the computational domain and its boundary. This latter relation holds separately for $\bar{\mathbf{u}}$ and $\mathbf{u}'$ provided that $\bar{w}$ and w' are defined appropriately (Zaron and Egbert, 2006b).

Table 4
Energy equation: boundary terms and integrals.

Term [units]	Prior	P1	P2
$\int_{\partial\mathcal{D}} u'p$ [GW]	1.06	0.97	0.97
$\max_{\partial\mathcal{D}} \|u'p\|$ [kW/m]	5.9	5.6	5.3
$\max_{\partial\mathcal{D}} \|\bar{u}\rho_o g\eta\|$ [kW/m]	91	91	92

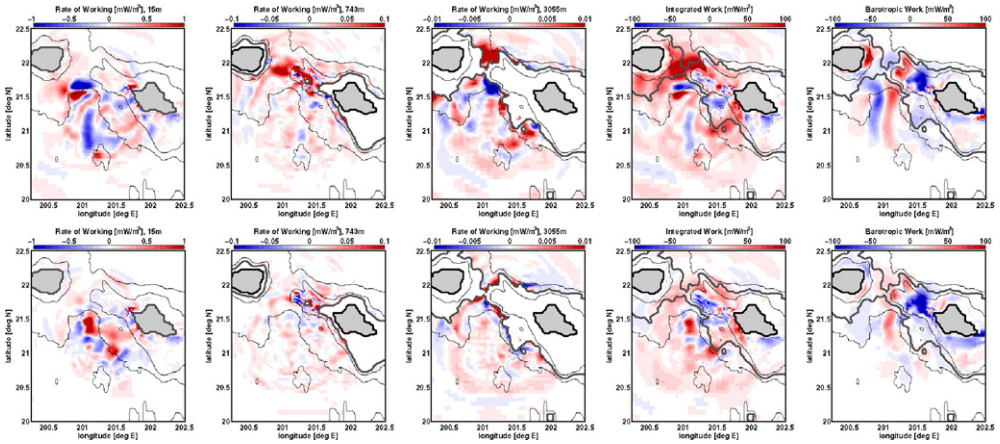

Fig. 15. Work done by residual forcing. Top row: P1 solution. Bottom row: P2 solution. Note different color scales and units. First three columns show baroclinic residual work, $\mathbf{u}' \cdot \hat{\boldsymbol{\upsilon}}^*$, near surface (15 m), lower-thermocline 743 m, and at depth (3055 m). The fourth column shows the vertical integral of baroclinic residual work. Last column is barotropic residual work $H\bar{\mathbf{u}} \cdot \hat{\boldsymbol{\upsilon}}^*$.

The values shown in the Table 3 have been computed from the finite-sum analogues to the volume-integrated energy equations, and the values have been scaled by ρ_o to yield energy in Joules. Also, note that the the sponge layer has been excluded from the volume integrals.

There are several important points to note from Table 3. First, the solver residuals ($\bar{\epsilon}$, ϵ', and ϵ^{APE}) are comparable to the explicitly modeled dissipative terms in all the solutions. This occurs because the primitive equations admit a narrow viscous-diffusive boundary layer scale which is not resolved in the simulations (Balmforth et al., 2002), so the solver residual is significant in the boundary layers along the internal wave characteristics. In spite of this, numerical experiments have demonstrated that the resolved fields, and volume integrals of the viscous and diffusive terms, are stably computed by PEZ-HAT (Zaron and Egbert, 2006b).

A second observation from Table 3 is that the forcing residual, i.e., the forcing correction necessary to make the model agree with the HFR observations, is never more than twice as large as the dissipative terms. Although the prior solution is rather different from the HFR data, the forcing corrections necessary to reconcile the model with the observed fields are modest. In spite of this, the large scale fields have been altered to reduce the radiated internal waves substantially. The baroclinic conversion rate (denoted $-b\bar{w}^*$) is reduced from 1.46 GW, in the prior model, to 1.11 GW in P1 and 1.22 GW in P2, reductions of 24% and 16%, respectively. The conversion of the barotropic tide into internal motions relies on a very delicate phase relationship between the currents and pressure field. Note from Table 4 that the barotropic wave energy flux ($\bar{u}\rho_o g\eta$) is approximately 90 kW/m, while the radiating baroclinic wave energy flux ($\max|u'p'|$) is around 5 kW/m; although, values as high as 15 kW/m occur near the conversion sites. The topography scatters a small fraction of the incident barotropic energy into baroclinic waves.

Fig. 15 shows the spatial structure of the work done by the residual forcing for the P1 and P2 solutions. As was shown in Fig. 13, the strongest model corrections occur near the ocean surface and in the vicinity of topographic slopes. The single feature common to both the P1 and P2 residuals is the barotropic dissipation on the shallowest part of Ka'ena Ridge, where the residual is about 50 mW/m^2. This is comparable to what one would expect in a turbulent bottom boundary layer, which would require $|u| \approx 0.1$ m/s to make $C_d|u|^3$ account for the residual forcing ($C_d = 2 \times 10^{-3}$ is assumed). In deeper water the residual work is comparable to what might be hypothesized for turbulent dissipation, but the residual acts to both accelerate and decelerate the flow so it cannot be simply an estimate of the frictional terms there.

4. Discussion

We have shown that the HFR surface velocity observations are consistent with the predictions of the regional primitive equations model when we account for plausible errors in both the model and the data. In the present case, the model errors are scaled by assuming they arise from interactions between the M_2 tide and the slowly varying background current. Taken at face value, this would suggest that mesoscale variability reduces the conversion of barotropic to baroclinic tides by about 20%, compared to what it would be in its absence. There are, however, some aspects of the data-assimilative solutions which are not consistent with tidal-mesoscale interactions. In this section we consider some additional factors.

The fact that the data-assimilative solution assigned nearly all of the residual forcing to the momentum equations, and essentially none to the mass equation, is inconsistent with our picture of internal wave propagation through a slowly varying mesoscale ambient. Kunze (1985) analyzed the dispersion relation for internal waves propagating through a quasi-geostrophic background and showed that the dominant interactions, aside from the Doppler shift, are determined by two terms. In the momentum equations, the interaction arises from varying the effective Coriolis frequency by the relative vorticity of the background flow; and in the mass equation, the straining of the waves by the thermal wind shear, $\mathbf{u} \cdot \nabla \bar{b}$, should be of first-order significance, approximately 20% of $|i\omega b|$. The data-assimilative solutions found here allocate essentially all of the model forcing error to the momentum equations, and none to the mass equation. In other words, the momentum equation residuals are comparable to the assumed model errors, while the residuals in the mass equation are much too small.

In fact, the data-assimilative algorithm has found just what was expected from such a "least-squares" formulation, namely, the smallest possible correction to the prior model which is consistent with the observed surface currents. Absent either (i) a more complete description of the covariance between the model forcing errors, $\hat{\boldsymbol{\upsilon}}$ and $\hat{\beta}$, or (ii) an improved estimate of the three-dimensional non-tidal fields, it is unlikely that the present approach to estimating the tidal fields could be substantially improved. At the present level of description, only corrections to the momentum equations are required.

Could other processes be responsible for the discrepancy between the prior model and the observations? A range of plausible alternatives is considered below.

4.1. Turbulent mixing

Direct observations of turbulence microstructure on the Hawaiian Ridge find that dissipation rates vary over the spring-neap cycle, but the average value in Kauai Channel ranges from 10^{-2} to 10^{-1} mW/m^3 over the uppermost 1000 m of the water column (Klymak et al., 2006). Turbulence dissipation is roughly a factor of 10 or more too small to account for the model residual near the ocean surface (see Fig. 15), but it is of the correct magnitude to explain the residual deeper in the water column.

4.2. Tidal self-interactions

One way to assess the M_2– M_2 interactions is to compute the Stokes velocity of the tidal currents (Longuet-Higgins, 1969), i.e., the tidal average of

$$\mathbf{u}_S = \int_0^t Re\{\mathbf{u}e^{i\omega t'}\}\,\mathrm{d}t' \cdot \nabla Re\{\mathbf{u}e^{i\omega t}\}, \tag{35}$$

and examine the relative magnitude of self-advection, $\mathbf{u}_S \cdot \nabla \mathbf{u}$, and the corrections to the momentum equations, $\hat{\boldsymbol{\upsilon}}$. We have computed this quantity (not shown) and find that the Stokes velocity reaches maximum values of 10 cm/s in the shallowest water over Ka'ena Ridge near Ka'ena Point. Over the deeper water, e.g., south-east of Kauai, the Stokes velocity is less than 1 cm/s, a factor of 10 or more too small to account for the model residual.

4.3. Temporal variability of the mesoscale

The model forcing error proposed in Eq. (30) is based on the assumption of a steady, but spatially varying, mesoscale eddy field; however, Chavanne et al. (submitted for publication-a) find significant temporal variation in semidiurnal band energy that is unrelated to the spring-neap cycle. These temporal variations in phase decorrelate on a time-scale between 10 and 20 days, so there are approximately 6 degrees of freedom in each of the 3-month periods, P1 and P2. It is difficult to quantify the impact

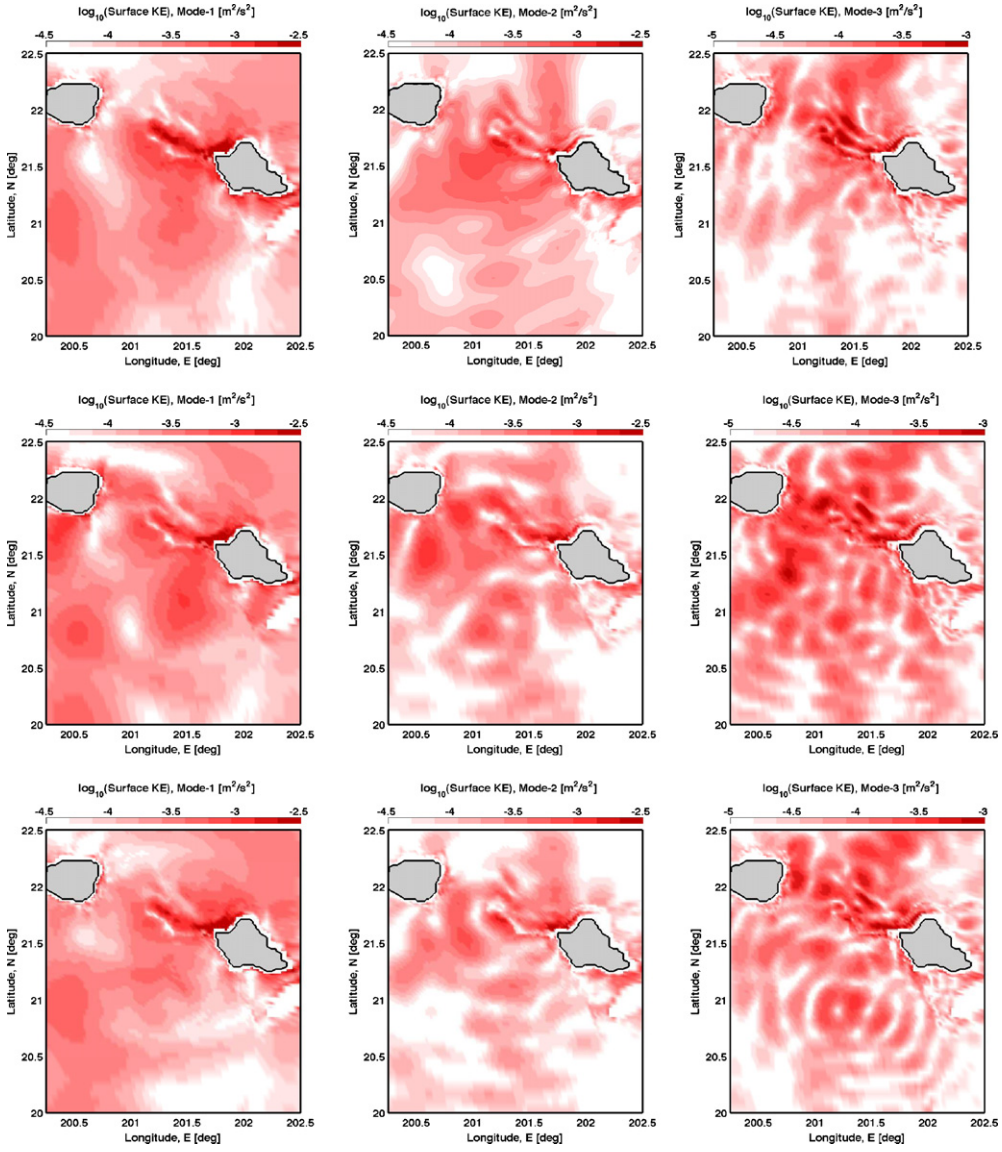

Fig. 16. Modal decomposition of surface kinetic energy. Top row: prior solution. Middle row: P1 solution. Bottom row: P2 solution. The velocity field from the solutions has been projected onto the flat-bottom vertical modes, and the surface kinetic energy for the first three internal modes is shown.

of this process, since the effect depends on the phase integrated along the (time-varying) ray paths. One crude estimate is simply to take the observed phase variation, about $\delta\theta_1 = 10^\circ = 0.27$ rad (cf., Fig. 14 of Chavanne et al., submitted for publication-a), and assign this entirely to mode-1, the largest-amplitude mode. The phase change of the $n > 1$ other modes can be estimated as $\delta\theta_n = c_n/c_1\delta\theta_1$, assuming phase variability is due to propagation path length changes. Random phase variations ought to reduce the coherent tidal variance by a factor $\nu_i^2 = 1 - \exp(-(\delta\theta)_i^2)$ (e.g., Colosi and Munk, 2006), and these values are tabulated in Table 1 for internal modes in water of 4000 m depth. Fig. 16 shows a modal decomposition of the surface kinetic energy for the prior and inverse solutions. These modes are the locally defined internal modes, which form a convenient basis for orthogonalizing the variance of the solutions; although, they are dynamically coupled where the bottom depth is not constant. It is evident that higher modes are increasingly modified in the inversions, but the changes are not simply proportional to a scalar factor, ν_i. Furthermore, the amplitude does not decay monotonically away from the generation sites as would be expected from simple phase decorrelation along ray paths. Thus, it does not appear that temporal variability in the background fields can simply explain the observed surface currents; although, the magnitude of the corrections increasing with mode number is broadly consistent with this process.

4.4. Bottom topography

As mentioned in Section 2.3, the bathymetry data which define the computational domain are certainly contaminated with error. Here again, it is difficult to conclusively evaluate impact of these errors on the model; however, there are two facts worth consideration. First, the solutions of the prior model are relatively insensitive to increased computational resolution. Higher resolution simulations (not shown) have more well-defined zones of elevated surface kinetic energy than those shown in Fig. 3. And, second, the changes in bathymetry necessary to effect a change from the prior to the observed surface current would involve major reconfigurations of the bathymetry over scales of at least 10 to 20 km, e.g., the scale of the displacement in the maximum of the surface kinetic energy. It seems unlikely that the bathymetry errors are sufficient to account for much of the difference between the prior and observed surface currents.

5. Conclusions

We have used a data-assimilating primitive equations model to assimilate HFR surface current observations in Kauai Channel, a site of intense baroclinic tidal generation. There are significant differences between the prior model and the observed currents, but these can be reconciled by admitting plausible corrections to the model to account for errors in the model physics, namely, the neglect of variations in the background stratification, advection, and turbulence mixing. These terms have been estimated by considering the influence of the slowly varying non-tidal (mesoscale) fields.

The amplitude of the model corrections is small. The residual forcing is largely confined to the upper 300 m of the water column in the viewing area of the HFR arrays. In other words, the discrepancy between the data-less prior model and the observations can be explained by upper-ocean processes near the observation sites. In the upper ocean these corrections are consistent with the estimated magnitude of tidal-mesoscale interaction, which are roughly 10 times larger than independent observations of turbulence dissipation (Klymak et al., 2006). The residual model forcing corrections deeper in the water are mostly confined near the ocean bottom at sites of strong cross-isobath flow where the baroclinic tidal generation occurs; however, the corrections are generally so small that we cannot distinguish them from numerical solver error.

Two data-assimilative solutions have been found during 3-month periods in 2002 (P1) and 2003 (P3). The tidal solutions during these periods are different in detail, but they have similar energetics. The barotropic tide loses energy at a rate of 1.1 GW during P1 and 1.2 GW during P2, the prior estimate being 1.5 GW. Considering that the numerical solver error is estimated to be about 10%, the differences in the energetics during these periods is not significant, but the reduction compared to the prior may be.

The estimation procedure has allowed us to dynamically interpolate and extrapolate the tidal fields which are consistent with the HFR surface currents. Unfortunately, we cannot unambiguously determine the energetic relationship between the tides and the mesoscale. The assimilation procedure, by design, finds the minimum residual forcing fields to bring the solution into agreement with the data. But it is only necessary to add forcing to the momentum equations, leaving the mass equation unadjusted. Consequently, the residual forcing fields are not dynamically consistent with the perturbations one would expect for internal wave propagating through a slowly variable ambient. Alternate explanations for the residual forcing were explored, the most likely alternative being tidal interactions with temporal variations in the background.

The next logical step for investigating tidal-mesoscale interactions must involve explicitly modeling both time scales. The challenge is to resolve the spatial scales which span from 2 km or less (Carter et al., 2008) at the generation site, to the 100 km scale of the mode-1 tide and mesoscale. Modeling the nonlinear self-interactions presumably requires high vertical resolution to represent the beams of tidal energy where kinetic energy is concentrated. Another challenge is the lack of detailed data at the mesoscales; an approach using altimeter data and an assumed modal projection may prove fruitful; although, Chavanne et al. (submitted for publication-b) find that simulated tidal-mesoscale interactions depend in detail on the vertical structure of the mesoscale. HFR surface currents are one of the few sources of oceanic data that resolves the spatial mesoscales while simultaneously resolving the tidal timescales. Efforts to assimilate these data in the time domain are ongoing.

Acknowledgements

Development of PEZ-HAT for data-assimilative modeling using the IOM was supported by the U.S. National Science Foundation (NSF) Information Technology Research grant ITR-121542; additional support to E.Z. and G.E. was provided by NSF grants OCE-9819518 (The Hawai'i Ocean Mixing Experiment, HOME) and OCE-0623540 (Regional Studies of the Internal Tide). The construction of the HF radars was supported by NSF Major Research Instrumentation grant OCE-9724464 and their deployment by NSF grants OCE-9819534 and OCE-0453848 (HOME) to P.F.; additional support to C.C. was provided by NSF grant OCE-0426112. This publication utilizes data from the Hawai'i Ocean Time Series, supported by NSF grant OCE-0327513. The ADCPs on the A2 mooring were deployed by Doug Luther, supported by NSF grant OCE-9819533 (HOME), and Murray Levine, supported by NSF grant OCE-9819532 (HOME). Richard Ray and Brian Beckley (NASA/GSFC) prepared the satellite altimetry data sets. Contribution number 7568 from the School of Ocean and Earth Science and Technology, University of Hawai'i at Manoa.

References

Alford, M.H., 2003. Redistribution of energy available for ocean mixing by long-wave propagation of internal waves. Nature 423, 159–162.

Andersen, O.B., Knudsen, P., 1997. Multi-satellite ocean tide modelling—the K_1 constituent. Prog. Oceanogr. 40, 197–216.

Arbic, B.K., Garner, S.T., Hallberg, R.W., Simmons, H.L., 2004. The accuracy of surface elevations in forward global barotropic and baroclinic tide models. Deep Sea Res. II 51, 3069–3101.

Baines, P.G., 1982. On internal tide generation models. Deep Sea Res. 29, 307–338.

Balmforth, N.J., Ierley, G.R., Young, W.R., 2002. Tidal conversion by nearly critical topography. J. Phys. Oceanogr. 32, 2900–2914.

Bennett, A.F., 2002. Inverse Modeling of the Ocean and Atmosphere. Cambridge University Press, United Kingdom.

Bennett, A.F., Chua, B.S., Pflaum, B.L., Erwig, M., Fu, Z., Loft, R.D., Muccino, J.C., 2008. The Inverse Ocean Modeling System. Part I. Implementation. J. Atm. Ocean. Tech. 25, 1608–1622.

Carter, G., 2006. Kauai channel bathymetric data, personal communication.

Carter, G.S., Gregg, M.C., 2006. Persistent near-diurnal internal waves observed above a site of M2 barotropic-to-baroclinic conversion. J. Phys. Oceanogr. 36, 1136–1147.

Carter, G.S., Merrifield, M.A., Becker, J., Katsumata, K., Gregg, M.C., Luther, D.S., Levine, M.D., Boyd, T.J., Firing, Y.L., 2008. Energetics of M_2 barotropic to baroclinic tidal conversion at the Hawaiian Islands. J. Phys. Oceanogr. 38, 2205–2223.

Chavanne, C., Flament, P., Carter, G., Merrifield, M., Luther, D., Zaron, E.D., Gurgel, K., submitted for publication-a. The surface expression of semi-diurnal internal tides in the Kauai Channel, Hawai'i. Part I. Observations and numerical predictions. J. Phys. Oceanogr.

Chavanne, C., Flament, P., Luther, D., Gurgel, K., submitted for publication-b. The surface expression of semi-diurnal internal tides in the Kauai Channel, Hawai'i. Part II. Interactions with mesoscale currents. J. Phys. Oceanogr.

Chiswell, S.M., 2006. Altimeter and current meter observations of internal tides: do they agree? J. Phys. Oceanogr. 36, 1860–1872.

Chua, B., Bennett, A.F., 2001. An inverse ocean modeling system. Ocean Model. 3, 137–165.

Colosi, J.A., Munk, W., 2006. Tales of the venerable Honolulu tide gauge. J. Phys. Oceanogr. 36, 967–996.
Dushaw, B.D., Egbert, G.D., Worcester, P.F., Cornuelle, B.D., Howe, B.M., Metzger, K., 1997. A TOPEX/POSEIDON global tide model TPXO.2 and barotropic tidal currents determined from long-range acoustic transmissions. Prog. Oceanogr. 40, 337–368.
Eakins, B., Robinson, J., Kanamatsu, T., Naka, J., Smith, J., Takahashi, E., Clague, D., 2003. Hawaii's volcanoes revealed. Technical report, U.S. Geological Survey, http://geopubs.wr.usgs.gov/i-map/i2809.
Egbert, G.D., Bennett, A.F., Foreman, M., 1994. TOPEX/POSEIDON tides estimated using a global inverse model. J. Geophys. Res. 99, 24821–24824.
Egbert, G.D., Erofeeva, S.Y., 2002. Efficient inverse modeling of barotropic ocean tides. J. Atm. Ocean. Tech. 19, 183–204.
Egbert, G.D., Ray, R.D., 2000. Significant tidal dissipation in the deep ocean inferred from satellite altimeter data. Nature 405, 775–778.
Egbert, G.D., Ray, R.D., 2001. Estimates of M_2 tidal energy dissipation from TOPEX/POSEIDON altimeter data. J. Geophys. Res. 106, 22475–22502.
Egbert, G.D., Ray, R.D., Bills, B.G., 2004. Numerical modeling of the global semidiurnal tide in the present day and in the last glacial maximum. J. Geophys. Res. 109, C03003.
Fujieki, L., Santiago-Mandujano, F., Hannides, C., Lukas, R., Karl, D., 2005. Hawaii Ocean Time-series Program Data Report 14, 2002. Technical report, School of Ocean and Earth Science and Technology, Univ. of Hawaii, Honolulu, HI.
Fujieki, L., Santiago-Mandujano, F., Hannides, C., Lukas, R., Karl, D., Fitzgerald, D., 2006. Hawaii Ocean Time-series Program Data Report 15, 2003. Technical report, School of Ocean and Earth Science and Technology, Univ. of Hawaii, Honolulu, HI.
Garrett, C., Kunze, E., 2007. Internal tide generation in the deep ocean. Annu. Rev. Fluid Mech. 39, 57–87.
Gerkema, T., 2006. Internal-wave reflection from uniform slopes: higher harmonics and Coriolis effects. Nonlin. Proc. Geophys. 13, 265–273.
Gurgel, K., Antonischki, G., Essen, H., Schlick, T., 1999. Wellen Radar (WERA), a new ground-wave based HF radar for ocean remote sensing. Coast. Eng. 37, 219–234.
Jayne, S.R., St. Laurent, L., 2001. Parameterizing tidal dissipation over rough topography. Geophys. Res. Lett. 28, 811–814.
Klymak, J.M., Moum, J.M., Nash, J.D., Kunze, E., Girton, J.B., Carter, G.S., Lee, C.M., Sanford, T.B., Gregg, M.C., 2006. An estimate of tidal energy lost to turbulence at the Hawaiian Ridge. J. Phys. Oceanogr. 36, 1148–1164.
Klymak, J.M., Pinkel, R., Rainville, L., 2008. Direct breaking of the internal tide near topography: Kaena Ridge, Hawaii. J. Phys. Oceanogr. 38, 380–399.
Kunze, E., 1985. Near-inertial wave propagation in geostrophic shear. J. Phys. Oceanogr. 15, 544–565.
Lee, C.M., Kunze, E., Sanford, T.B., Nash, J.D., Merrifield, M.A., Holloway, P.E., 2006. Internal tides and turbulence along the 3000-m isobath of the Hawaiian Ridge with model comparisons. J. Phys. Oceanogr. 36, 1165–1183.
Legg, S., Huijts, K.M., 2006. Preliminary simulations of internal waves and mixing generated by finite-amplitude tidal flow over isolated topography. Deep Sea Res. II 53, 140–156.
Levine, M.D., Boyd, T.J., 2006. Tidally-forced internal waves and overturns observed on a slope: results from the HOME survey component. J. Phys. Oceanogr. 36, 1184–1201.
Llewellyn Smith, S.G., Young, W.R., 2002. Conversion of the barotropic tide. J. Phys. Oceanogr. 32, 1554–1566.
Longuet-Higgins, M.S., 1969. On the transport of mass by time varying ocean currents. Deep Sea Res. 16, 431–448.
Merrifield, M.A., Holloway, P.E., 2002. Model estimates of M_2 internal tide energetics at the Hawaiian Ridge. J. Geophys. Res. 107.
Muccino, J.C., Arango, H., Bennett, A.B., Chua, B.S., Cornuelle, B., DiLorenzo, E., Egbert, G.D., Hao, L., Levin, J., Moore, A.M., Zaron, E.D., 2008. The inverse ocean modeling system. II. Applications. J. Atm. Ocean. Tech. 25, 1623–1637.
Munk, W.H., Wunsch, C., 1998. Abyssal recipes II: energetics of tidal and wind mixing. Deep Sea Res. 45, 1977–2010.
Nash, J.D., Kunze, E., Lee, C.M., Sanford, T.B., 2006. Structure of the baroclinic tide generated at Kaena Ridge, Hawaii. J. Phys. Oceanogr. 36, 1123–1135.
Niwa, Y., Hibiya, T., 2004. Three-dimensional numerical simulation of M_2 internal tides in the East China Sea. J. Geophys. Res. 109.
Pacanowski, R.C., Gnanadesikan, A., 1998. Transient response in a z-level ocean model that resolves topography with partial cells. Mon. Wea Rev. 126, 3248–3270.
Pacanowski, R.C., Griffies, S.M., 1999. The MOM3 Manual. Technical report, NOAA/Geophysical Fluid Dynamics Laboratory.
Pawlowicz, R., Beardsley, B., Lentz, S., 2002. Classical tidal harmonic analysis including error estimates in MATLAB using T_TIDE. Comput. Geosci. 28, 929–937.
Pearson, R.A., 1974. Consistent boundary conditions for numerical models of systems that admit dispersive waves. J. Atmos. Sci. 31, 1481–1489.
Petrelis, F., Llewellyn Smith, S.G., Young, W.R., 2006. Tidal conversion at a submarine ridge. J. Phys. Oceanogr. 36, 1053–1071.
Purser, R.J., Wu, W.-S., Parrish, D.F., Roberts, N.M., 2003. Numerical aspects of the application of recursive filters to variational statistical analysis. Part II. Spatially inhomogeneous and anisotropic general covariances. Mon. Wea Rev. 131, 1536–1548.
Rainville, L., Pinkel, R., 2006. Propagation of low-mode internal waves through the ocean. J. Phys. Oceanogr. 36, 1220–1236.
Ray, R., Mitchum, G.T., 1997. Surface manifestation of internal tides in the deep ocean: observations from altimetry and island gauges. Prog. Oceanogr. 40, 13–162.
Ray, R.D., Mitchum, G.T., 1996. Surface manifestation of internal tides generated near Hawaii. Geophys. Res. Lett. 23, 2101–2104.
Rudnick, D.L., Boyd, T.J., Brainard, R.E., Carter, G.S., Egbert, G.D., Gregg, M.C., Holloway, P.E., Klymak, J.D., Kunze, E., Lee, C.M., Levine, M.D., Luther, D.S., Martin, J.P., Merrifield, M.A., Moum, J.N., Nash, J.D., Pinkel, R., Rainville, L., Sanford, T.B., 2003. From tides to mixing along the Hawaiian Ridge. Science 301, 355–357.
Shchepetkin, A.F., McWilliams, J.C., 2005. The regional ocean modeling system (ROMS): a split-explicit, free-surface, topography-following-coordinate oceanic model. Ocean Model. 9, 347–404.
Simmons, H.L., Hallberg, R.W., Arbic, B.K., 2004a. Internal wave generation in a global baroclinic tide model. Deep Sea Res. II 51, 3043–3068.
Simmons, H.L., Jayne, S.R., St. Laurent, L.C., Weaver, A.J., 2004b. Tidally driven mixing in a numerical model of the ocean general circulation. Ocean Model. 6, 245–263.
Sirkis, Z., Tziperman, E., 1997. Finite difference adjoint or adjoint of finite difference? Mon. Wea Rev. 125, 3373–3378.

St. Laurent, L.C., Nash, J.D., 2004. An examination of the radiative and dissipative properties of deep ocean internal tides. Deep Sea Res. II 51, 3029–3042.
Vecchia, A.V., 1985. A general class of models for stationary two-dimensional random processes. Biometrika 72, 281–291.
Whittle, P., 1954. On stationary processes in the plane. Biometrika 41, 434–449.
Zaron, E.D., Egbert, G.D., 2006a. Estimating open-ocean barotropic tidal dissipation: the Hawaiian Ridge. J. Phys. Oceanogr. 36, 1019–1035.
Zaron, E.D., Egbert, G.D., 2006b. Verification studies for a z-coordinate primitive-equation model: tidal conversion at a mid-ocean ridge. Ocean Model. 14, 257–278.
Zaron, E.D., Egbert, G.D., 2007. The impact of the internal tide on data-assimilative model estimates of the surface tide. Ocean Model. 18, 210–216.
Zilberman, N.V., Merrifield, M.A., Carter, G.S., Luther, D.S., Levine, M.D., Boyd, T.J., 2008. Time-variable conversion of barotropic to baroclinic M_2 tidal energy at the Kaena Ridge, in preparation.